Project No: 603502

**DACCIWA**

"Dynamics-aerosol-chemistry-cloud interactions in West Africa"

# Deliverable

# D4.2 Model evaluation

| | |
|---|---|
| **Due date of deliverable:** | 30/11/2016 |
| **Completion date of deliverable:** | 30/11/2016 |
| **Start date of DACCIWA project:** | 1st December 2013 **Project duration:** 60 months |
| **Version:** | [V1.0] |
| **File name:** | [D4.2_ Model_evaluation _DACCIWA_v1.0.pdf] |
| **Work Package Number:** | **4** |
| **Task Number:** | **2** |
| **Responsible partner for deliverable:** | **KIT** |
| **Contributing partners:** | **UNIVMAN** |
| **Project coordinator name:** | Prof. Dr. Peter Knippertz |
| **Project coordinator organisation name:** | Karlsruher Institut für Technologie |

**The DACCIWA Project is funded by the European Union's Seventh Framework Programme for research, technological development and demonstration under grant agreement no 603502.**

| Dissemination level | | |
|---|---|---|
| **PU** | Public | **x** |
| **PP** | Restricted to other programme participants (including the Commission Services) | |
| **RE** | Restricted to a group specified by the consortium (including the Commission Services) | |
| **CO** | Confidential, only for members of the consortium (including the Commission Services) | |

| Nature of Deliverable | | |
|---|---|---|
| **R** | Report | **x** |
| **P** | Prototype | |
| **D** | Demonstrator | |
| **O** | Other | |

## DOCUMENT INFO

### Authors


| Author | Beneficiary Short Name | E-Mail |
|---|---|---|
| Bernhard Vogel | KIT | Bernhard.vogel@kit.edu |
| Konrad Deetz | KIT | Konrad.deetz@kit.edu |
| Hugh Coe | UNIVMAN | hugh.coe@manchester.ac.uk |
| John Marsham | UNIVLEEDS | J.Marsham@leeds.ac.uk |
| Philip Rosenberg | UNIVLEEDS | P.D.Rosenberg@leeds.ac.uk |
| Tanja Stanelle | ETH Zurich | tanja.stanelle@env.ethz.ch |
| Angela Benedetti | ECMWF | Angela.Benedetti@ecmwf.int |
| Laurent Menut | UPMC | menut@lmd.polytechnique.fr |
| Adrien Deroubaix | UPMC | adrien.deroubaix@lmd.polytechnique.fr |


### Changes with respect to the DoW

| Issue | Comments |
|---|---|

### Dissemination and uptake

| Target group addressed | Project internal / external |
|---|---|
| Scientific community | Internal and external |

### Document Control

| Document version # | Date | Changes Made/Comments |
|---|---|---|
| V0.1 | 21.10.2016 | First draft of KIT to discuss with UNIVLEEDS and UNIVMAN |
| V0.2 | 11.11.2016 | Synthesis of the information from the different contributors |
| V1.0 | 15.11.2016 | Version for approval by the GA |
| V2.0 | 28.11.2016 | Final version including the comments from the GA |
| | | |

# Table of Contents

# 1. Introduction

This report provides an overview about the aerosol/chemistry models in weather forecast and climate mode related to WP4 focusing on aerosol-cloud properties, including model characteristics, the pre-DACCIWA performance and their adaptations to the needs within DACCIWA. By focusing on the nocturnal low-level stratus clouds (NLLS hereafter) and the spatiotemporal aerosol and trace gas distribution, the model performances are assessed and compared along the models and with observational data if available. Due to the postponement of the DACCIWA field campaign from June/July 2015 to June/July 2016 only a small amount of observations is available for the use in this report. Therefore the study mainly relates to remote sensing data and AERONET observations. Regarding the NLLS, the regional extent, depth, cloud top height as well as the diurnal cloud transition (including transition onset) from full stratus cover to the break up and development of cumuli. For model realizations with extended time periods, the frequency of occurrence of the NLLS is analyzed. The spatiotemporal distribution of aerosol and trace gases, whose reasonable representation is mandatory for a robust interpretation of the aerosol-cloud interactions, is considered in addition.
Section 2 gives a general overview about the used models and the model realization used for this study. In Section 3 all models were introduced consecutively more in detail together with the assessment of the model performance. Key figures were given to support the findings. The report closes with the summary and discussion of the overall model performances.

# 2. Overview about models and used model datasets

This study includes five models which have been applied in research mode (see Tab. 2.1). The models are highly diverse regarding their representation of cloud microphysics and aerosols-chemistry but also regarding the setup and the available simulated time periods. This will impede the intercomparison between the models. Table 2.2 gives an overview about the model realizations used for assessing the model performance in Section 3.

**Tab. 2.1** – Model overview

| Model name | Model version used in DACCIWA | Mode | Contact person |
|---|---|---|---|
| COSMO-ART | COSMO5.1-ART3.1 | research | Konrad Deetz |
| UM | UM | research | Philip Rosenberg |
| CHIMERE | CHIMERE2016a | research | Laurent Menut |
| ECHAM-HAM | ECHAM6.3-HAM2.3 | research | Tanja Stanelle |
| IFS-CAMS | IFS-CAMS | research | Angela Benedetti |

In total 13 dataset from D1 to D13 were used for the assessment of the model performances. The grid mesh sizes cover a wide range from 2.5 to 200 km. Whereas COSMO-ART, UM, CHIMERE and IFS-CAMS run in weather forecast mode, ECHAM-HAM runs in climate mode.

**Tab. 2.2** – Model realizations used for model performance assessment in Section 3

| Model name | DACCIWA related model datasets used for this study | | | |
|---|---|---|---|---|
| | Time period | Simulation domain | Grid size (km) | Dataset |
| COSMO-ART | 01.06.-31.07.2016 | 25°W - 40°E, 20°S - 35°N | 28 | D1 |
| | 02.07.2016 | 20°W - 17°E, 3°S - 23°N | 5 | D2 |
| | 02.07.2016 | 10°W - 12°E, 0°S - 15°N | 2.5 | D3 |
| UM | 27.06.-17.07.2016 | 8°W – 15°E, 4°S-16°N | 4.4 | D4 |
| CHIMERE | 01.05.-29.07.2014 | 25°W – 55°E, 20°S – 35°N | 60 | D5 |
| | 01.05.-29.07.2014 | 8°W – 18°E, 5°S – 15°N | 20 | D6 |
| ECHAM-HAM | 1996-2010 | global | 200 | D7-D11 |
| IFS-CAMS | 01.06.-31.07.2014 | global | 80 | D12, D13 |

# 3. Model performances

In the following section the five models presented in Tab. 2.1 are introduced in detail regarding their model characteristics together with the adaptations made for DACCIWA. Subsequently the model performance is illustrated by figures based on the datasets presented in Tab. 2.2. Every single model section closes with conclusions made from the dataset analysis. For spatial averages a common domain is defined including the area from 8°W-8°E and 5°N-10°N (*Box 1* hereafter, see Fig. 3.1).

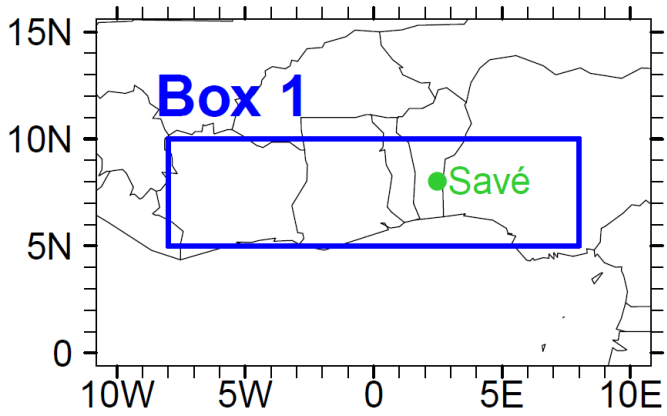


**Fig. 3.1** – Definition of a common area for spatial averages (Box 1, from 8°W-8°E and 5°N-10°N) which denotes the central research domain of DACCIWA.

## 3.1 COSMO-ART

### 3.1.1 Model description

COSMO-ART (Consortium for Small-scale Modeling – Aerosols and Reactive Trace gases) is a comprehensive online-coupled model system (Vogel et al., 2009) based on the operational weather forecast model COSMO (Baldauf et al., 2011). COSMO-ART includes a comprehensive chemistry module to describe the gaseous composition of the atmosphere and secondary aerosol formation. It allows for feedback of the simulated aerosol particles with radiation, cloud formation and precipitation (e.g. Stanelle et al., 2010, Athanasopoulou et al., 2014; Rieger et al., 2014; Walter et al., 2016).
The size distribution of aerosol within COSMO-ART is approximated by log-normal distributions (modes hereafter). Table 3.1.1 summarized all 11 modes of COSMO-ART together with their initial median diameters, standard deviations and chemical compositions.

**Tab. 3.1.1** – Chemical composition, initial diameter and standard deviation of the lognormal distributions of the 11 modes in COSMO-ART (AIT: Aitken mode, AITS: Aitken mode containing a soot core, ACC: accumu-lation mode, ACCS: accumulation mode containing a soot core, SOOT: pure soot mode, SEASA: sea salt fine, SEASB: sea salt medium, SEASC: sea salt coarse, SOILA: mineral dust fine, SOILB: mineral dust medium, SOILC: mineral dust coarse)

| | AIT | AITS | ACC | ACCS | SOOT | SEASA | SEASB | SEASC | SOILA | SOILB | SOILC |
|---|---|---|---|---|---|---|---|---|---|---|---|
| Soot | | ■ | | ■ | ■ | | | | | | |
| Sulfate | ■ | ■ | ■ | ■ | | ■ | ■ | ■ | | | |
| Ammonium | ■ | ■ | ■ | ■ | | | | | | | |
| Nitrate | ■ | ■ | ■ | ■ | | | | | | | |
| Organics | ■ | ■ | ■ | ■ | | | | | | | |
| Water | ■ | ■ | ■ | ■ | | ■ | ■ | ■ | | | |
| Sodium chloride | | | | | | ■ | ■ | ■ | | | |
| Initial diameter µm) | | | | | | | | | | | |
| Number | 0.01 | 0.08 | 0.07 | 0.08 | 0.08 | 0.2 | 2 | 12 | 0.64 | 3.5 | 8.7 |
| Mass | | | | | | | | | 1.5 | 6.7 | 14.2 |
| Standard deviation | | | | | | | | | | | |
| | 1.7 | 1.7 | 2 | 2 | 1.4 | 1.9 | 2 | 1.7 | 1.7 | 1.6 | 1.5 |

The standard deviation is kept constant while the median diameter of the aerosol changes during transport. Chemical reactions are calculated with RADMKA (Regional Acid Deposition Model Version Karlsruhe; Vogel et al., 2009), which is based on RADM2 (Regional Acid Deposition Model, Stockwell et al., 1990).

The formation of secondary organic aerosol is calculated by a VBS approach (volatility basis set; Athanasopoulou et al., 2013). COSMO-ART explicitly treats the aging of soot particles transferring them from external to internal mixtures as described in Riemer et al. (2004). The radiative fluxes are calculated with the GRAALS radiation scheme (Ritter and Geleyn, 1992). A priori Mie calculations have been performed for the initial aerosol particle size distributions and their chemical composition to obtain mass-specific values for the extinction coefficient, single scattering albedo, and asymmetry parameter. These coefficients also depend on wavelength. To consider the optical properties of the current aerosol distribution the mass-specific parameters obtained by the Mie calculation are weighted with the mass fraction of the chemical components. Within COSMO-ART a full two-moment cloud microphysics scheme (Seifert and Beheng, 2006) is used. Aerosol activation is considered according to Fountoukis and Nenes (2005). Ice nucleation is based on the parametrization by Phillips et al. (2008). Cirrus formation and the competition between homogeneous and heterogeneous freezing is specified according to Barahona and Nenes (2009a, b).

COSMO-ART is able to describe the emission and atmospheric dispersion of natural (mineral dust, sea salt, volcanic ash, biogenic volatile organic compounds and pollen) and anthropogenic pollutants (anthropogenic emissions e.g. from traffic or industry, biomass burning emissions including a plume rise model (Walter et al., 2016) and flaring emissions).

Prior studies with COSMO-ART have shown the feasibility to assess the influence of aerosols on radiation and clouds in many regions and regarding different aerosol species. Stanelle et al. (2010) studied two dust storms over West Africa in March 2006 and June 2007 and quantified the averaged net shortwave radiation reduction with -140 W $m^{-2}$ during noon and the averaged net longwave radiative increase with +70 W $m^{-2}$ for an AOD (450nm) of 1. A case study of fire periods in Greece during late summer 2007 indicates a negative net radiative budged of up to -10W $m^{-2}$ with a temperature reduction over land of -0.5K (Athanasopoulou et al., 2014). Walter et al. (2016) derived for the direct aerosol effect below a biomass burning aerosol layer from Canadian wild forest fires at

15 July 2010 a 2m temperature reduction up to 6K. The temperature within the smoke layer was increased, which lead to an increase in atmospheric stability. A study of convective cumulus clouds developing after the passage of a cold front on 25 April 2008 over Germany, considering the presence of online calculated sea salt concentrations instead of prescribed aerosol climatologies, indicated a significant change in cloud properties such as cloud droplet radii and number concentrations, including a systematic decrease in precipitation rate of the post-frontal cumulus clouds (Rieger et al., 2014).

### 3.1.2 Adaptations for DACCIWA

To apply COSMO-ART to the conditions of SWA, several adaptations have been realized. The global EDGAR emission database was preprocessed for COSMO-ART and the biogenic emission routine MEGAN2.1 of Guenther et al. (2012) was implemented into COSMO-ART, allowing the state-of-the-art calculation of the biogenic emissions of isoprene, limonene and alpha-pinene depending on current meteorological (radiation and temperature) and land surface (leaf area and plant functional types) conditions.

Since gas flaring seems to be a relevant source of pollution, Nigeria is with 15 billion cubic meter flared gas the second largest flaring country (World Bank, 2012), we have developed a flaring emission inventory (Deetz and Vogel, 2016, under review). This inventory allows for a physically based estimation of the flaring emissions of carbon dioxide, carbon monoxide, sulphur dioxide, nitrogen monoxide and nitrogen dioxide based on combustions calculations and remote sensing observations. Therefore, the inventory is highly resolved in space and time and available for recent times in contrast to other inventories. We have processed flaring inventories for June-July 2014 and June-July 2015. As soon as the necessary data will be available also the time period of the DACCIWA field campaign June-July 2016 will be analyzed according to the flaring emissions.

Additionally, we have further developed our mineral dust emission routine. By combining the parameterization of Vogel et al. (2009) and Shao et al. (2010) the emission routine can now be flexible applied globally compared to the previous scheme in COSMO-ART. Results for the performance of the mineral dust parameterization are presented in Section 3.1.3. The external emission dataset for oceanic dimethyl sulfide (DMS) was updated using Lana et al. (2011). In COSMO-ART the DMS emission depends on wind speed. In summary COSMO-ART considers the following emissions within the DACCIWA studies: mineral dust, sea salt, dimethyl sulfate, biogenic volatile organic compounds as well as anthropogenic trace gases and aerosols (including biomass burning and flaring). Not considered are $NO_x$ emissions from lightning and soil. For anthropogenic emissions we use EDGAR HTAP V2 (EDGAR, 2010) and for the biomass burning emissions the CAMS Global Fire Assimilation System (GFAS, 2016), which is available near real-time.

For COSMO we use the tropical setup with includes among others an increased number of vertical levels up to 30km.

### 3.1.3 Dataset analysis

Within DACCIWA, COSMO-ART simulations for the three domains Continental, SWA and Regional were realized with a grid mesh size of 28, 5 and 3 km, respectively (see Fig. 3.1.1). As a part of the DACCIWA measurement campaign (June-July 2016) and especially the aircraft campaign (27 June to 17 July 2016, Aircraft special observing period (ASOP)) COSMO-ART operational aerosol/chemistry forecasts were realized from 8 May to 31 July 2016.

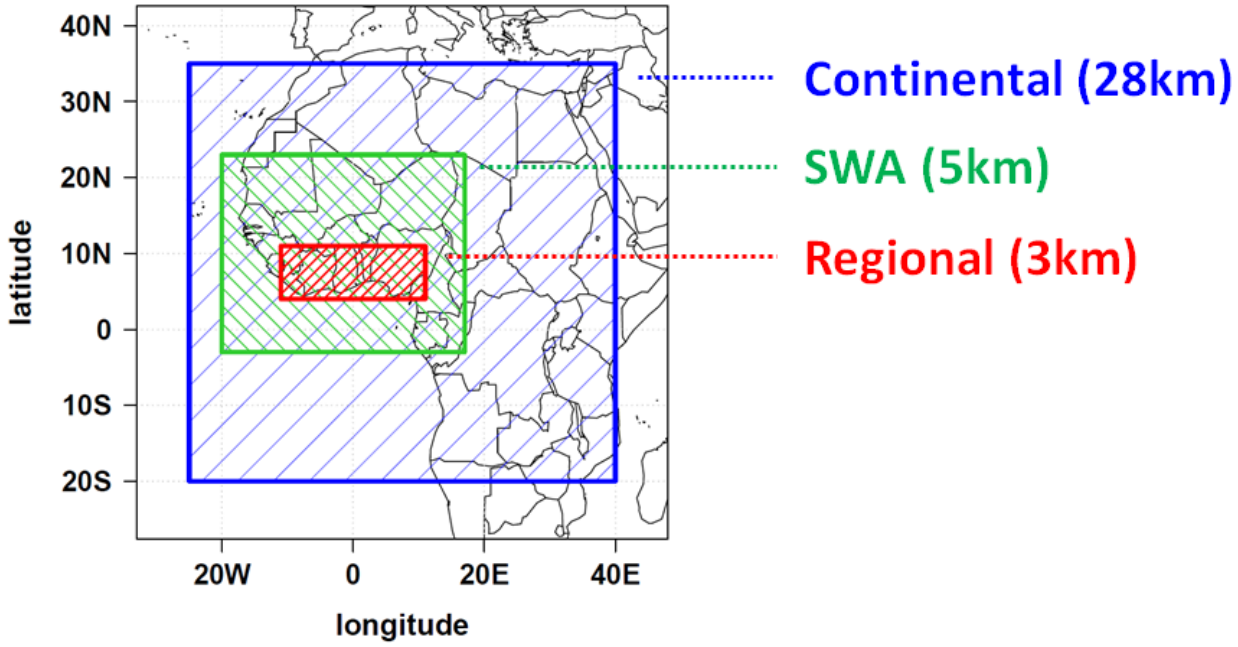


**Fig. 3.1.1** – Simulation domains applied for the COSMO-ART simulations. The blue, green and red domain refers to D1, D2 and D3 respectively (see Tab. 3.1.1).

With that we intended to support the decision-making of the flight planning during the campaign. The forecast visualization was regularly uploaded to the campaign server dacciwa.sedoo.fr (http://dacciwa.sedoo.fr/source/indexItem.php?current=20161109&nav=COSMO-ART) which can also be used for post-campaign decisions about case studies. As meteorological driver, ICON forecasts were provided by the German Weather Service. The COSMO-ART dataset D1 (1 June to 31 July, see Tab.3.1.2) is a part of this forecast time period, without taking into account interactions of aerosols with cloud and radiation.

**Tab. 3.1.2** – Characteristics of the COSMO-ART model datasets used for this study

| Characteristics | Dataset D1 | D2 | D3 |
|---|---|---|---|
| Time period | 01.06.-31.07. 2016 | 02.07.2016 | 02.07.2016 |
| Simulation domain | 25°W – 40°E, 20°S – 35°N | 20°W – 17°E, 3°S – 23°N | 10°W – 12°E, 0°S – 15°N |
| Grid mesh size (km) | 28 | 5 | 2.5 |
| Number of vertical levels | 50 | 50 | 80 |
| Meteorological boundary conditions | ICON | from D1 | from D2 |
| Convection parameterization | yes | yes | no |
| Cloud microphysics | one-moment bulk | one-moment bulk | two-moment |
| Aerosol type (online/prescribed) | mineral dust (online), sea salt (online), anthropogenic (prescribed) | mineral dust (online), sea salt (online), anthropogenic (prescribed) | mineral dust (online), sea salt (online), anthropogenic (prescribed) |
| Aerosol treatment (bulk/modal/sectional) | modal | modal | modal |
| Direct aerosol effect | climatology | climatology | with prognostic aerosol |
| Indirect aerosol effect | prescribed CCN | prescribed CCN | with prognostic aerosol |
| Chemical boundary conditions | MOZART | from D1 | from D2 |
| Chemistry (online/prescribed, full chemistry) | online, full chemistry | online, full chemistry | online, full chemistry |

Based on these forecasts we are focusing on a detailed case study from 2 July to 6 July, since this time period is linked to extensive observational data and widespread nocturnal low-level stratus (NLLS). The first nest into the Continental domain (SWA, see green box in Fig. 3.1.1) differs from the Continental domain only regarding the domain size and grid mesh size. The second nest (Regional, see red box in Fig. 3.1.1) includes several changes in the setup. This includes a higher number of vertical levels (80 instead of 50), the two-moment microphysics scheme and it considers

the direct and indirect aerosol effect. For this study we have selected the 2 July 2016 for the first nesting (D2, see Tab.3.1.1) and the second nesting (D3, see Tab.3.1.1).
Figure 3.1.2 shows the diurnal cycle of the cloud coverage profile, averaged over the time period 27 June to 17 July 2016 (ASOP) and Box 1 (see Fig. 3.1). By focusing on the lower troposphere (Fig. 3.1.2b) the evolution of the NLLS below 500m height above ground level can be seen, beginning with low values at midnight (black), 10% at 3 UTC (grey), 15% at 6 UTC (light blue) and approx. 10-30% at 9UTC (blue). After 9 UTC the maximum of the cloud cover shifts to higher altitudes, which is linked to a transition from stratus to cumulus clouds. The curve for 9 UTC is highlighted as dashed line because at this time the maximum of the NLLS occurs, which is in agreement with previous model studies (e.g. Schuster et al., 2013) and observations at Savé (see Fig. 3.1) during the DACCIWA measurement campaign.

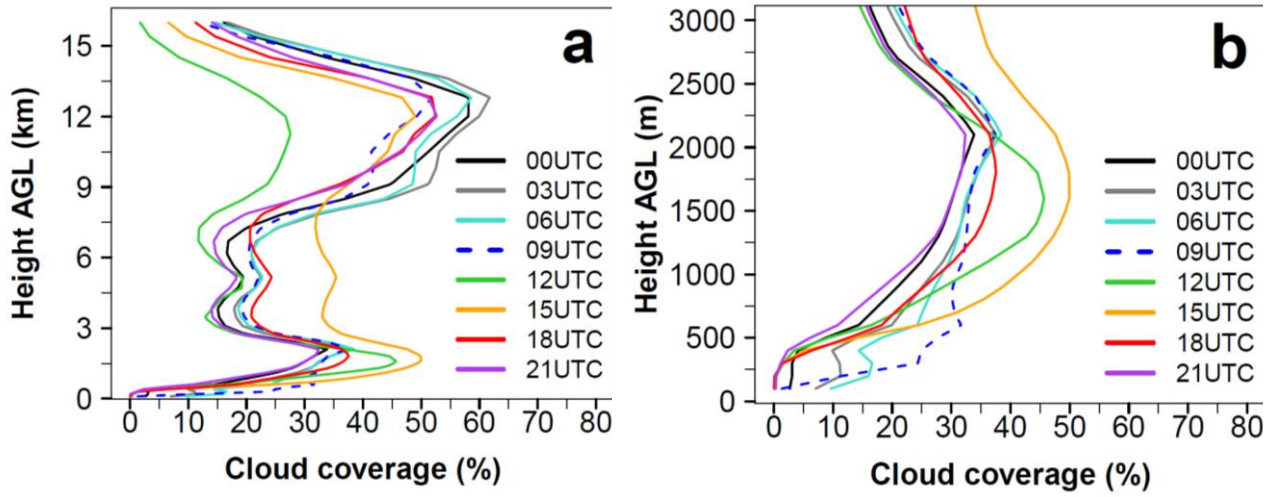


**Fig. 3.1.2** – Diurnal cycle of cloud coverage profile (in %) spatially averaged over Box 1 and temporally averaged from 27 June to 17 July 2016 for (a) 0-16km height above ground level (AGL) and (b) between 0-3km height AGL. 9 UTC (blue), which is known as the time of maximum extension of NLLS, is highlighted as dashed line. (D1)

Figure 3.1.3 is the same as Figure 3.1.2 but for cloud liquid water (in g $kg^{-1}$). Figure 3.1.3b reveals that the time of the highest stratus cloud coverage (9UTC) is also the time of the highest amount of cloud liquid water at this level. In Figure 3.1.2b and 3.1.3b also a slight increase in the height of the stratus can be seen from 0 UTC to 9 UTC. The stratus is lifted before the transition to cumulus takes place.

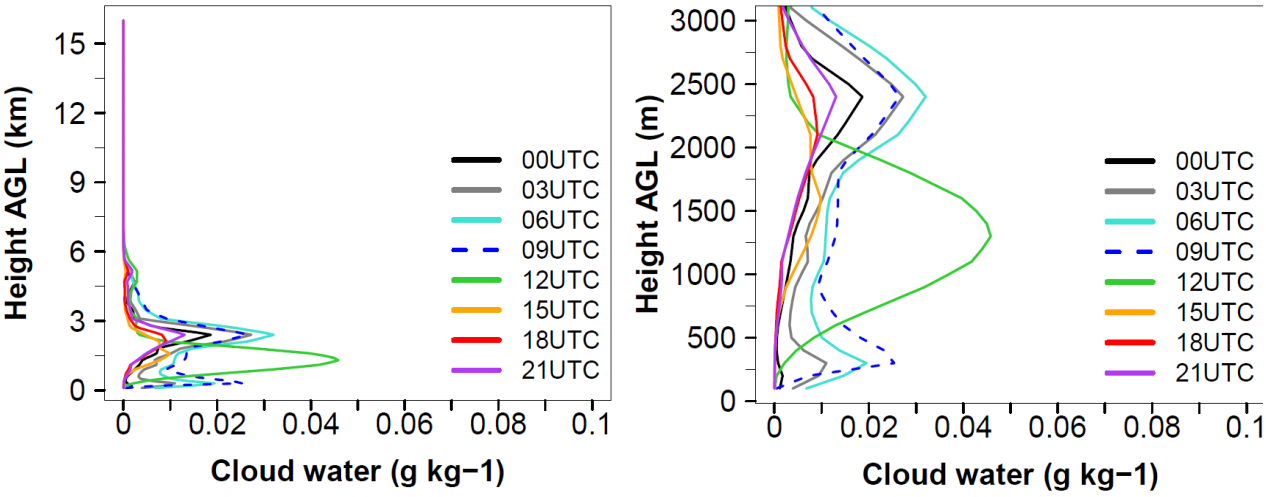


**Fig. 3.1.3** – As Fig.3.1.2 but for cloud liquid water (in g $kg^{-1}$). (D1)

In Figure 3.1.4a presents the mean diurnal cycle of the spatial extension of low clouds by vertically integrating the cloud liquid water in the lowest 2000m. From 0 UTC to 12 UTC a clear increase in the cloud water is visible and with the transition to cumulus a reduction of cloud liquid water from 15 UTC on, occurs. In the Save area the maximum occurs at 9 UTC and at 12 UTC already a reduction can be seen in central Ghana and southern Togo and Benin. The stratus first develops near the coast at 3 UTC and then going further inland. This development is especially noticeable over Ivory Coast with a development from southwest to northeast. The cloud water spatial distribution compares well with the cloud cover spatial distribution presented by Schuster et al. (2013) who conducted a WRF simulation for JAS 2006. For qualitative comparison Figure 3.1.4b shows the diurnal cycle of the mean low cloud cover.

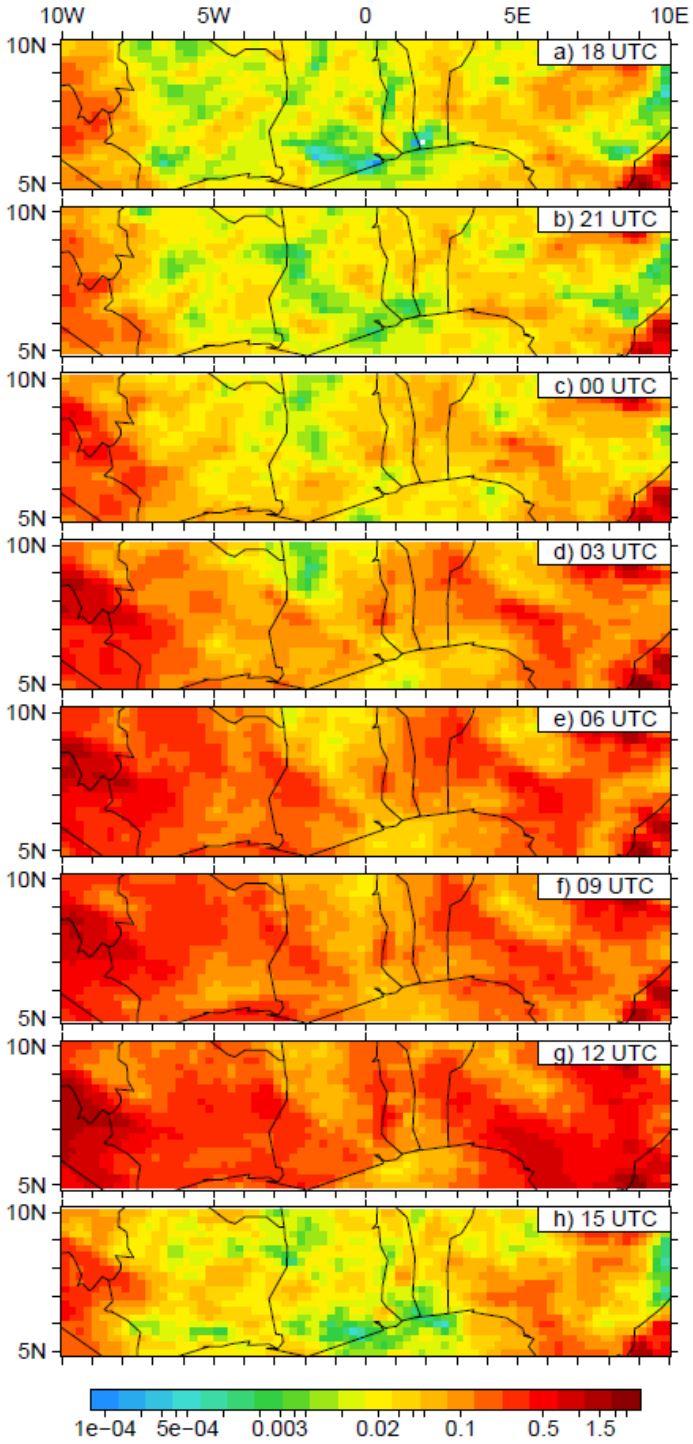


**Fig. 3.1.4a** – Diurnal cycle of vertically integrated cloud liquid water (in g $kg^{-1}$) spatial distribution below 2000m within Box 1, temporally averaged from 27 June to 17 July 2016. (D1)

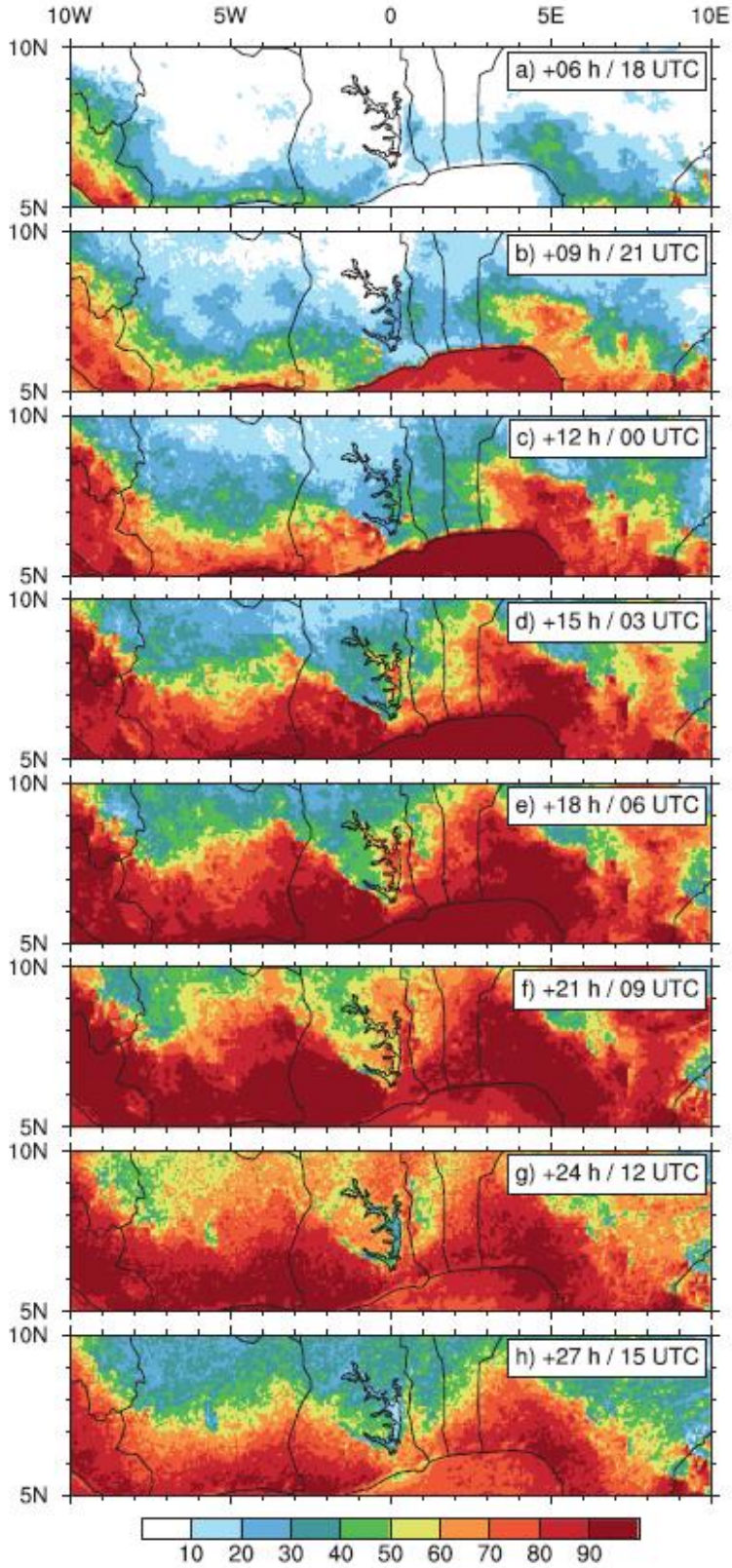


**Fig. 3.1.4b** – Diurnal cycle of low-level cloud cover (%) averaged over 90 daily model runs during the period JAS 2006 based on WRF simulations (**Schuster et al., 2013**).

The mean diurnal cycle of the cloud liquid water profile over Savé (ASOP time period) is shown together with the ceilometer cloud base measurements at Savé Supersite (horizontal bars). The black bars denote the mean low cloud base below 2000m in the same time period and the grey bars the absolute minimum values detected in this time.

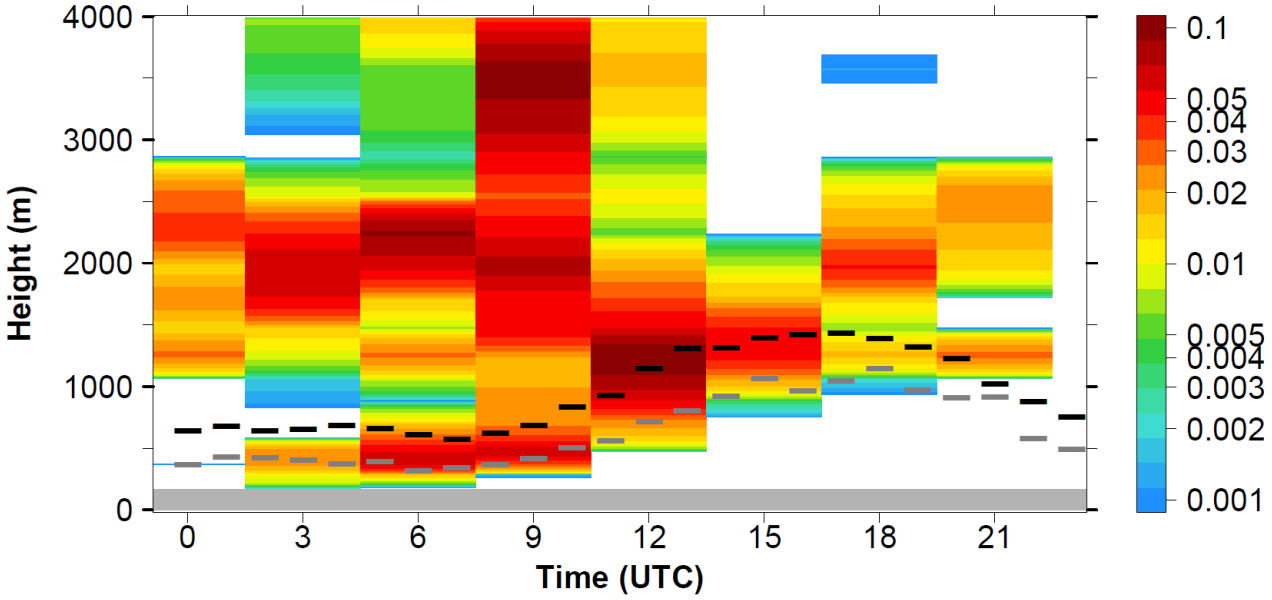


**Fig. 3.1.5** – Diurnal cycle of cloud liquid water (in g $kg^{-1}$) over Savé as shaded contour and Savé Supersite cloud base measurements as horizontal bars (hourly averages), temporally averaged from 27 June to 17 July 2016. Black bars show the temporal mean of observed cloud bases below 2000m (low clouds) and grey bars the absolute minimum cloud base in the time period. (D1)

The observed cloud base corresponds very well with the COSMO-ART simulations both in the absolute values and the evolution. At 3UTC the stratus development is visible with a very low cloud base around 250-500m. This stratus intensifies and slowly lifts from 3 to 9 UTC. After 9 UTC the transition to cumulus occurs, which is linked to a higher cloud base around 500-1000m. However, the reason for the high amount of cloud water between 1500m and 2000m between 0 UTC and 6 UTC and even higher reaching at 9 UTC is up to now not clear, since the Savé Supersite rather observed clear sky conditions around noon and rarely midlevel clouds in the early morning. From the lowest cloud liquid water layer visible between 3 and 9 UTC we can roughly estimate the cloud base (top) of the NLLS as approx. 0-400m (500-900m) AGL. Therefore, the vertical extent of the NLLS seems to be below 1000m.

The diurnal cycle of the frequency of occurrence of NLLS within ASOP is assessed via Figure 3.1.6 by detecting the number of days where the cloud liquid water at 500m AGL is greater equal a threshold of 0.005 g $kg^{-1}$ (red), 0.01 g $kg^{-1}$ (green) and 0.05 g $kg^{-1}$ (blue). Considering the red curve and by focusing on 9UTC, NLLS occurs on 81% of the days within ASOP. The high frequency of occurrence of NLLS can be confirmed from the eye observations at Savé Supersite. Days without stratus were an absolute exception. The study of Schuster et al. (2013) shows a frequency of the event “low-level cloud cover larger than 50%” for 9 UTC around 70% considering the time period 18-27 July 2006.

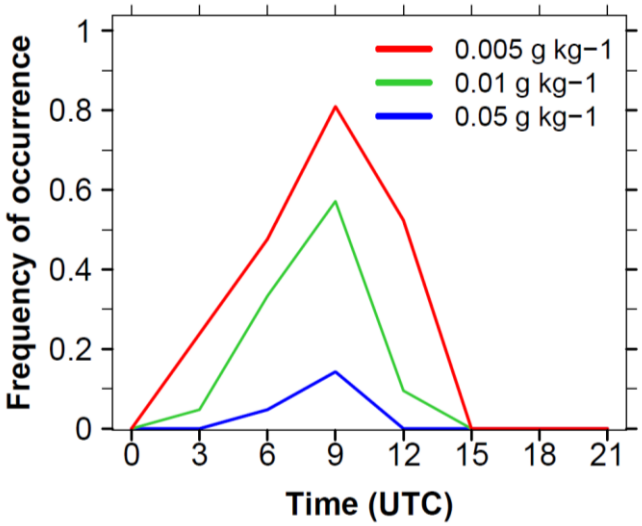


**Fig. 3.1.6** – Diurnal cycle of mean frequency of occurrence of cloud liquid water greater equal 0.005 g $kg^{-1}$ (red), 0.01 g $kg^{-1}$ (green) and 0.05 g $kg^{-1}$ (blue) at 500m AGL, considering the time period from 27 June to 17 July 2016, spatially averaged over Box 1. (D1)

Figure 3.1.7 shows a transect through a cloud area over Ghana on 2 July 2016 at 12 UTC considering cloud liquid water (Fig. 3.1.7a) and specific cloud droplet number concentration (Fig. 3.1.7b). This result refers to the dataset D3 of the second nesting which includes the aerosol direct and indirect effect. We plan to scale the aerosol number concentration regarding the aerosol indirect effect to quantify the influence of different aerosol concentrations on cloud characteristics. Since we currently work on these simulations, no comparison between different simulations for the Regional domain can be shown.

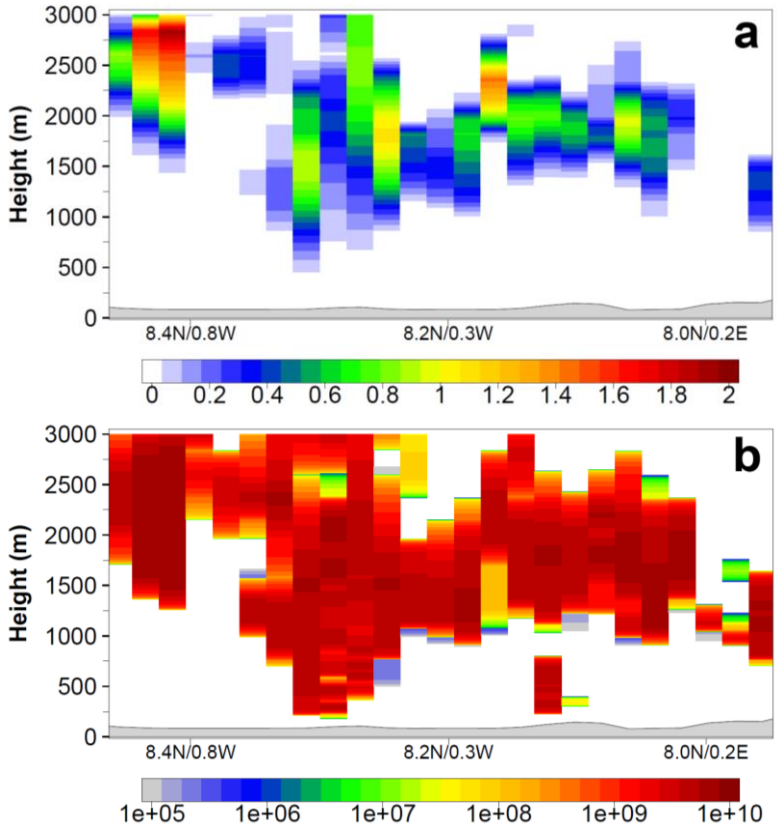


**Fig. 3.1.7** – Transects across a cloud area: (a) cloud liquid water (in g $kg^{-1}$) and (b) specific cloud droplet number ($kg^{-1}$) for 2 July 2016 at 9 UTC considering direct and indirect aerosol effect. (D3)

But a comparison for the specific day 2 July 2016 between the three domains of Fig.3.1.1 can be presented. Figure 3.1.8 shows (in the same structure as Fig. 3.1.3) the 2 July 2016 as it is simulated by D1 (Fig. 3.1.8a, 28km), D2 (Fig. 3.1.8b, 5km) and D3 (Fig. 3.1.8c, 2.5km).

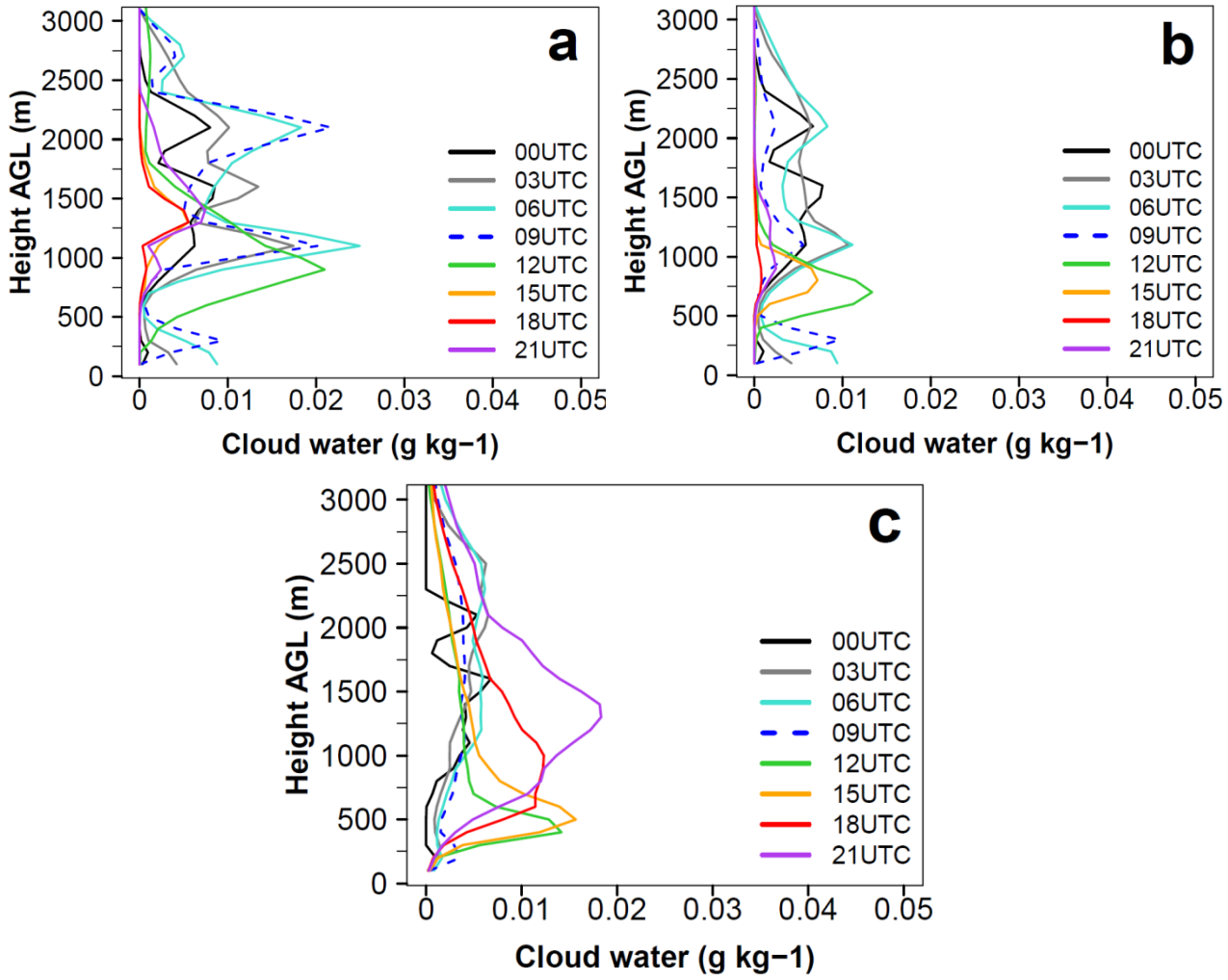


**Fig. 3.1.8** – Diurnal cycle of cloud liquid water profile (in g $kg^{-1}$) spatially averaged over Box 1 for 2 July 2016 between 0-3km AGL for (a) D1, (b) D2 and (c) D3. 9 UTC (blue), which is known as the time of maximum extension of NLLS, is highlighted as dashed line.

By focusing on the lowest 500m, the cloud liquid water vertical and temporal distribution is very similar for (a) and (b) but different for (c) which includes the two-moment microphysics and the aerosol-cloud and radiation interactions. It seems that these mechanisms reduce the cloud water in the lowest layer in the morning hours and shifts the daytime maximum of the cloud water to lower heights. These effects are up to now difficult to assess. Further simulations are necessary to isolate the responsible mechanisms.

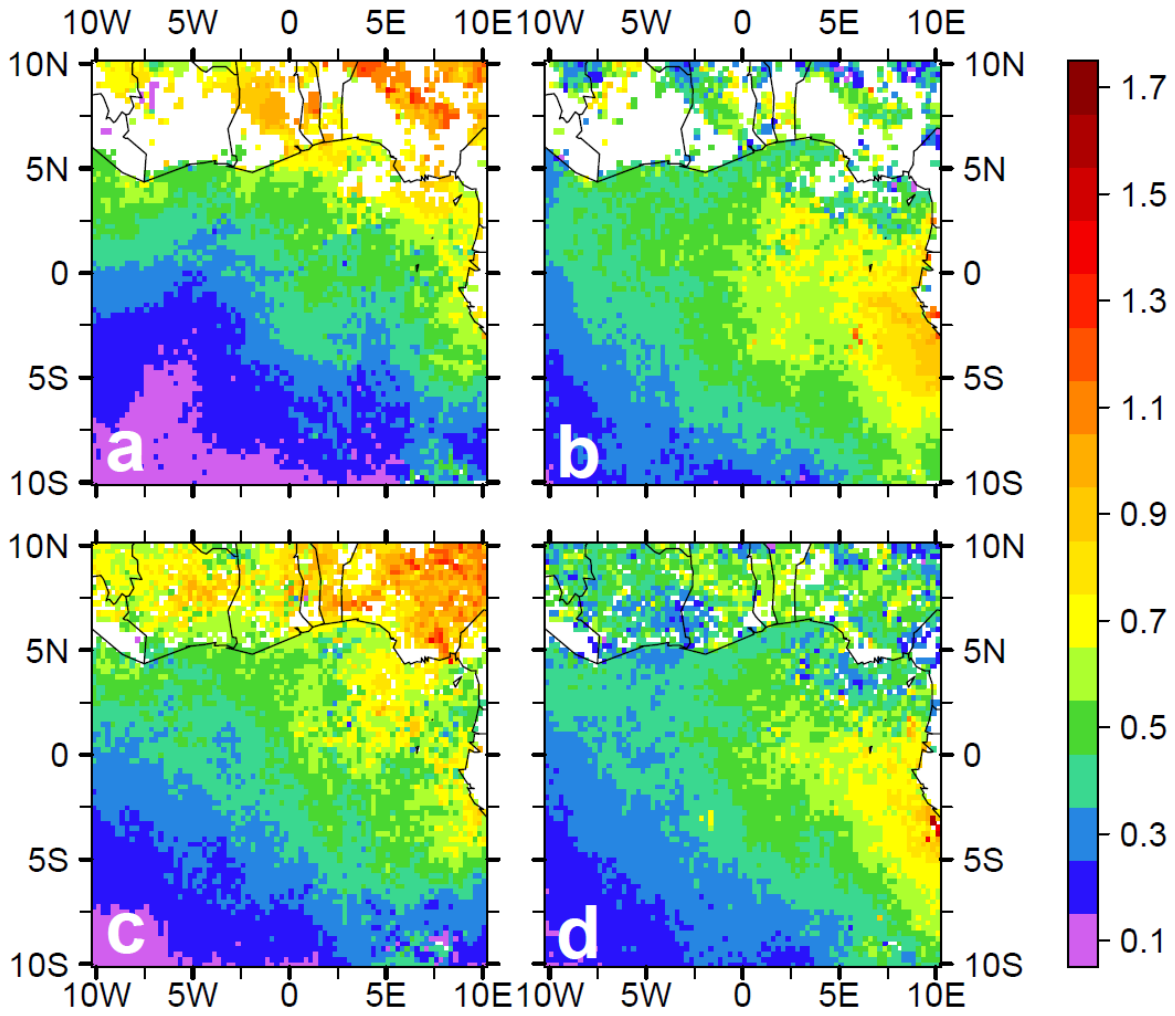


**Fig. 3.1.9** – Total AOD, temporally averaged from 27 June to 17 July 2016. (a) COSMO-ART spatiotemporally collocated with the available remote sensing observations of MODIS Terra, (b) MODIS Terra, (c) COSMO-ART spatiotemporally collocated with the available remote sensing observations of MODIS Aqua and (d) MODIS Aqua. (D1)

In addition to the analysis of the meteorology also the evaluation of the aerosol/chemistry is important to ensure that the cloud microphysics sees a reasonable aerosol concentration. Figure 3.1.9 therefore shows the comparison of the total AOD at 550nm simulated by COSMO-ART (Fig. 3.1.9a,c) and observed by MODIS Terra (Fig. 3.1.9b) and MODIS Aqua (Fig. 3.1.9d) regarding the ASOP time period. For Figure 3.1.9a the COSMO-ART results are spatiotemporally collocated to MODIS Terra (Fig. 3.1.9b) and for Figure 3.1.9c the COSMO-ART results are spatiotemporally collocated to MODIS Aqua (Fig. 3.1.9d.). In the MODIS observations the biomass burning emission plume is clearly visible. By calculating the anomaly of (a) and (b) (see Fig. 3.1.10a) and (c) and (d) (see Fig. 3.1.10b), a distinct overestimation of the simulated AOD over land can be seen. It is likely that the uncertainty in the anthropogenic emission is responsible for these differences.

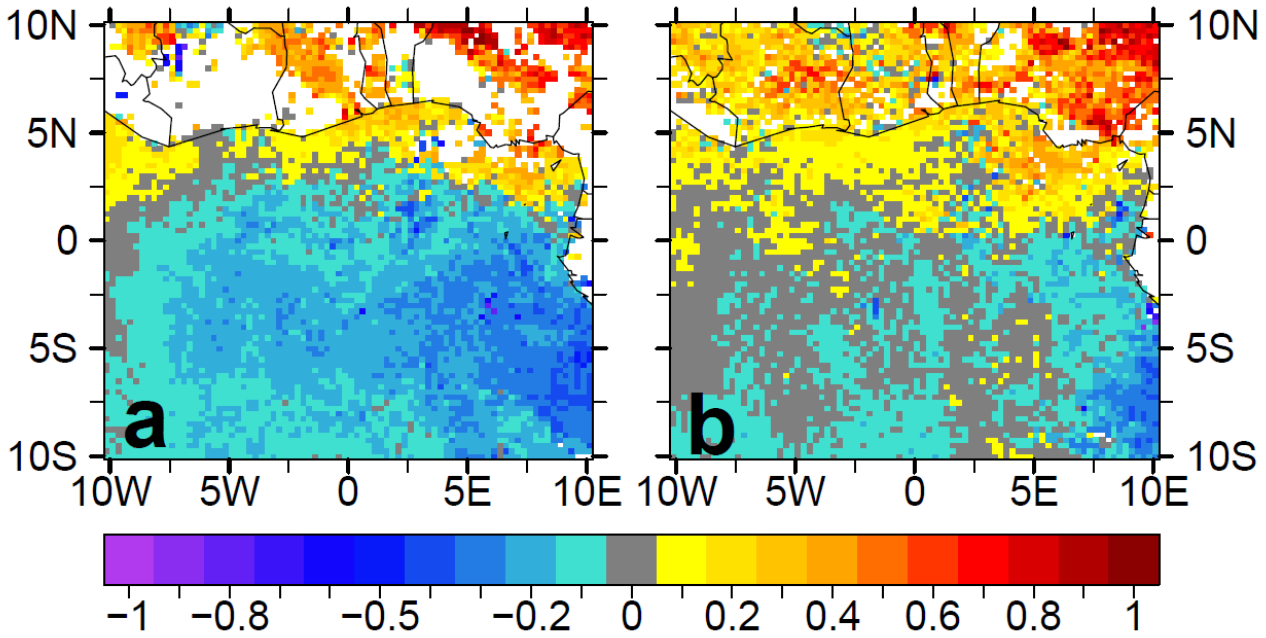


**Fig. 3.1.10** –AOD anomaly (a) COSMO-ART minus MODIS Terra (Fig. 3.1.9a minus Fig. 3.1.9b) and (b) COSMO-ART minus MODIS Aqua (Fig. 3.1.9c minus Fig. 3.1.9d), based on temporally averaged data from 27 June to 17 July 2016. (D1)

By using the results of the Copernicus Atmosphere Monitoring Service (CAMS) forecasts the total AOD can be separated into several components. CAMS itself will be introduced more in detail in Section 3.5.1. The total AOD is separated in Figure 3.1.11 in the mineral dust AOD (Fig. 3.1.11a), the sea salt AOD (Fig. 3.1.11b) and the anthropogenic aerosol AOD (Fig. 3.1.11c) for the time period from 13 June to 31 July 2016 over Savé. The mineral dust AOD simulated by COSMO-ART correlates excellently with CAMS, especially by considering the overall uncertainties within mineral dust emission parameterizations. For sea salt COSMO-ART shows higher AOD values compared to CAMS but the overall contribution of the sea salt AOD is one order of magnitude smaller than for the mineral dust. The largest differences occur for the anthropogenic AOD (Fig. 3.1.11c) as expected. In this case COSMO-ART has significant higher AOD values in comparison to CAMS. For the interpretation one has to keep in mind that the COSMO-ART part of Figure 3.1.11 refers to the COSMO-ART forecasts (D1) which were conducted without any assimilation. Aside from the initial and boundary conditions these forecasts were free-running in contrast to CAMS. CAMS routinely corrects the bias regarding the MODIS AOD (see Section 3.5.1). Therefore it is plausible that CAMS performs better towards MODIS than COSMO-ART.

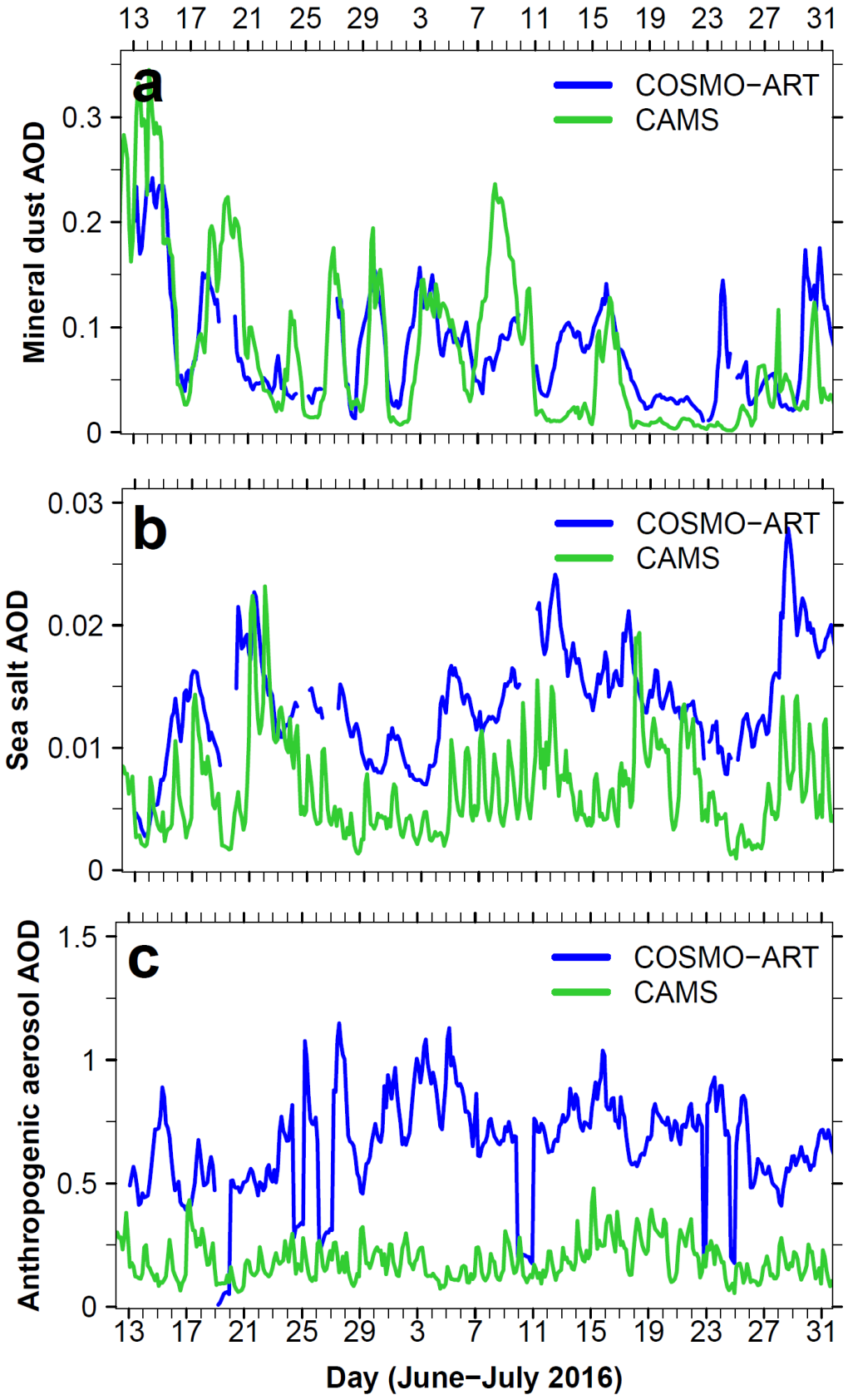


**Fig. 3.1.11** – AOD time series at Savé from 1 June to 31 July 2016 for (a) mineral dust, (b) sea salt and (c) anthropogenic aerosol simulated by COSMO-ART (blue) and CAMS (green). (D1)

In addition to Figures 3.1.9-3.1.11, which focus on aerosols, the Figures 3.1.12, 3.1.13 and 3.1.14 consider the mean trace gas concentrations for (a) COSMO-ART and (b) CAMS, i.e. the surface near ozone, $NO_x$ and isoprene concentration, respectively.

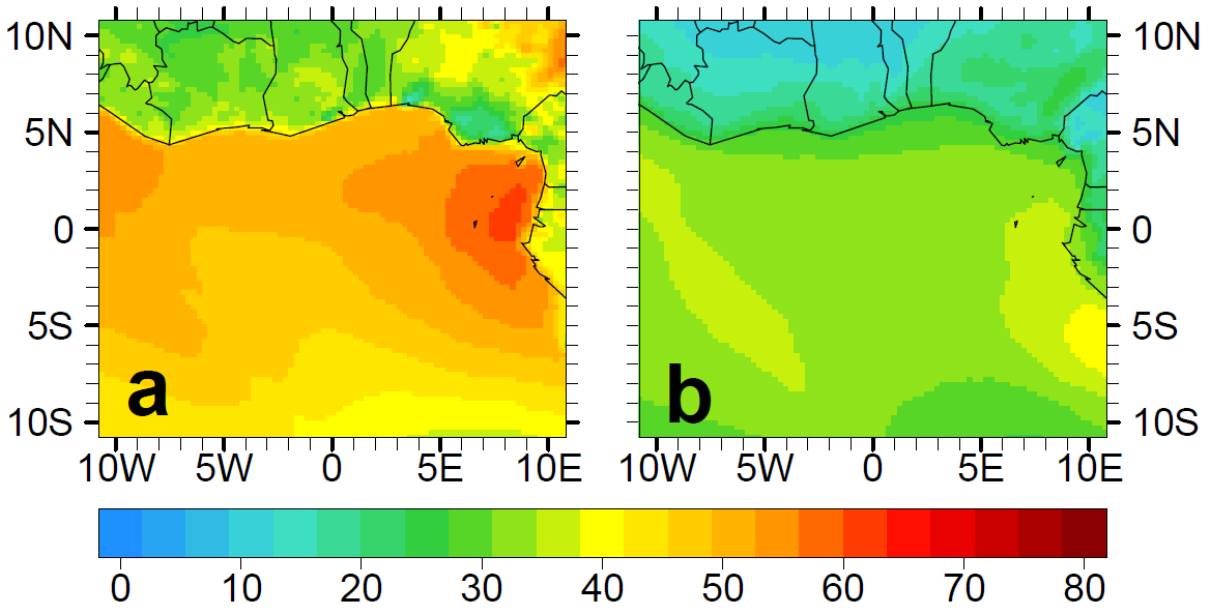


**Fig. 3.1.12** – Surface near ozone concentration (in ppbv), temporally averaged from 27 June to 17 July 2016 for (a) COSMO-ART and (b) CAMS. (D1)

For ozone and $NO_x$ COSMO-ART shows higher concentrations than CAMS, with a factor of about two for ozone and 3 for $NO_x$ by focusing on Benin. It is assumed that the uncertainty in the anthropogenic emissions lead to these differences.

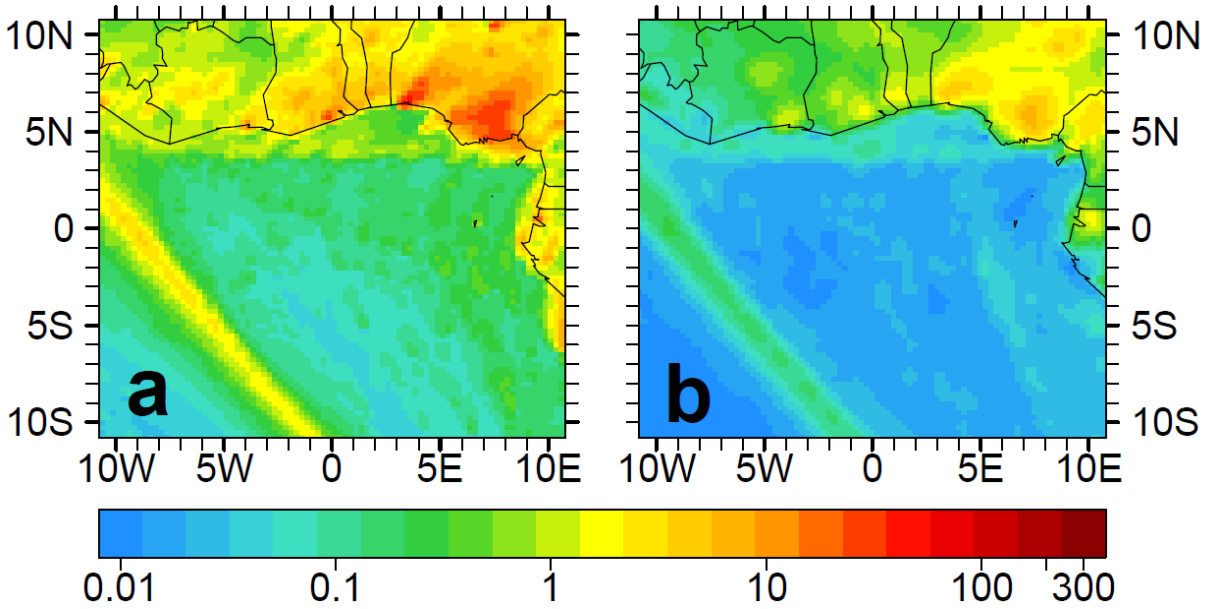


**Fig. 3.1.13** – Surface near NOx concentration (in ppbv), temporally averaged from 27 June to 17 July 2016 for (a) COSMO-ART and (b) CAMS. (D1)

The species isoprene is emitted from anthropogenic and biogenic sources. In case of isoprene the concentrations are smaller compared to CAMS. For COSMO-ART the highest values can be found in regions with a high fraction of vegetation (e.g. southern Ivory Coast and southern Ghana). The

evaluation of the distribution of aerosols and trace gases lead to the conclusion that more effort is necessary to reduce the uncertainty in the anthropogenic emissions. The new emission inventory for SWA, which will be provided by WP4, could be a step forward for a better emission representation.

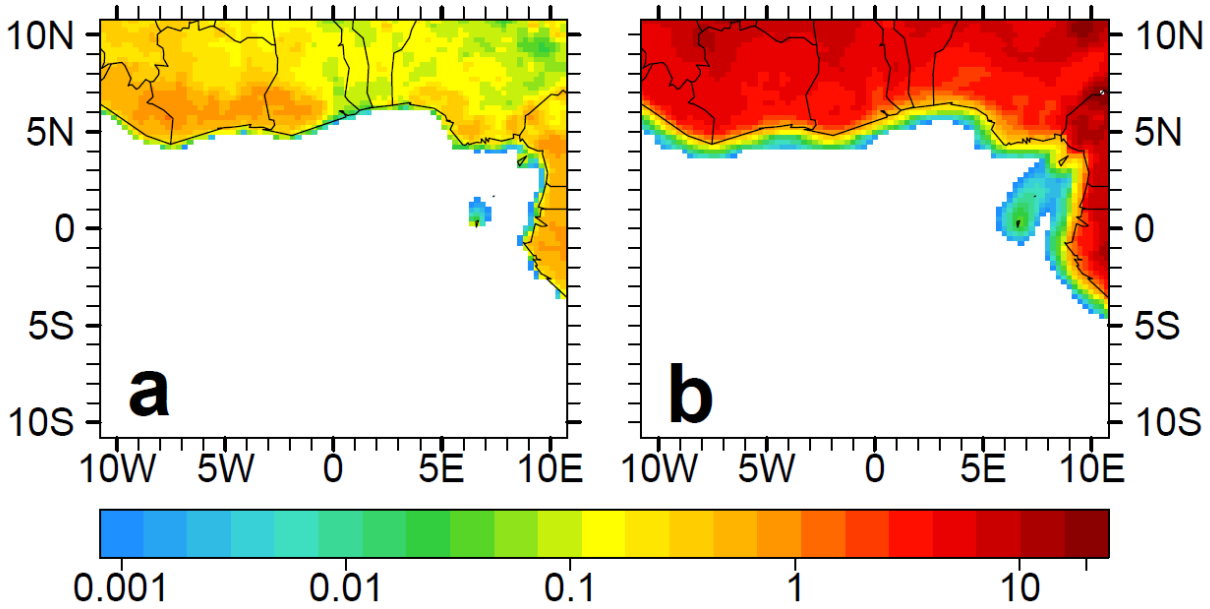


**Fig. 3.1.14** – Isoprene concentration at 1000hPa (in ppbv), temporally averaged from 27 June to 17 July 2016 for (a) COSMO-ART and (b) CAMS. (D1)

### 3.1.4 Conclusion

By using COSMO-ART we have assessed the cloud as well as aerosol/chemistry characteristics across SWA using the three datasets D1 (28km grid mesh size, 1 June to 31 July 2016), D2 (5km grid mesh size, 2 July 2016) and D3 (2.5km grid mesh size, 2 July 2016) (see Tab. 3.1.2 for further information on the data). The two-month dataset of D1 allows for statistics on the aerosol and cloud properties in contrast to the specific case studies of D2 and D3. By focusing on the three week time period of the ASOP (27 June to 17 July 2016) we have assessed the characteristics of the low clouds in terms of the cloud base, regional extent, diurnal transition and frequency of occurrence. In addition the spatiotemporal distribution of aerosols and trace gases across SWA has been analyzed. However, the authors note that D1 does not include any interaction between aerosols and clouds or radiation. D1 is part of the operational forecasts with COSMO-ART, which were conducted during the DACCIWA measurement campaign. Considering the computing time, concessions have to be made to deliver the forecast on time. To reflect this shortcoming, a double-nesting to a grid mesh size of 2.5km (D3) was realized which takes into account the direct and indirect aerosol effect.

The COSMO-ART results indicate a NLLS development starting at 3 UTC, reaching the maximum at 9 UTC and change then to fair weather cumulus clouds. The cloud base of the NLLS (approx. 0-400m AGL) increases slightly between 3 and 9 UTC and more rapidly after 9 UTC (approx. 1000-1500m AGL). This is in good agreement with previous model studies (Schuster et al., 2013) and observations from the Savé Supersite during the DACCIWA measurement campaign. The mean cloud top of the NLLS we roughly estimated as 500-900m AGL. Up to now we cannot validate this estimation but WP1 is planning to derive the cloud top from cloud radar and frequent radiosounding data measured at Savé Supersite. The spatial extent of low clouds is extensive, covering nearly completely the Box 1 defined in Fig. 3.1. The maximum is reached at 9 UTC. After 12 UTC the cloud liquid water below 2000m is strongly reduced compared to forenoon. The frequency of occurrence of NLLS within ASOP is assessed by using the threshold exceedance of cloud liquid water at 500m AGL (averaged over Box 1). During the maximum of the NLLS at 9 UTC, 81% of the days show a

cloud liquid water content greater equal 0.005 g $kg^{-1}$. The study of Schuster et al. (2013) shows a frequency of the event “low-level cloud cover larger than 50%” for 9 UTC around 70% considering the time period 18-27 July 2006.
The use of the two-moment microphysics scheme and by allowing for aerosol direct and indirect effect (D3), significant changes in the diurnal cycle of the cloud liquid water profile become evident. In the lowest 750m the cloud water is reduced in the morning hours and increased in the afternoon. Whether these changes are related to the two-moment microphysics, the aerosol interaction or a synergy of both is up to now not clear.
In addition we have compared the spatiotemporal distribution of aerosols and trace gases with remote sensing (MODIS) and operational chemistry model data (CAMS). The AOD (550nm) comparison with MODIS reveals a significant overestimation over land for COSMO-ART. By using CAMS, the AOD comparison can be separated in the AOD resulting from mineral dust, sea salt and anthropogenic aerosol. Best agreement is reached for mineral dust. For anthropogenic aerosol COSMO-ART is on average a factor of 3 higher than CAMS. It is supposed that the missing data assimilation in COSMO-ART (in contrast to CAMS) and the uncertainty in the anthropogenic emission dataset lead to the differences.
With the model setup described in Section 3.1.2 and by using the Regional domain (2.5km), the detailed interactive aerosol case study simulations (2-6 July 2016) will be continued to finally come to more robust conclusions regarding the aerosol-cloud properties across the research area.

## 3.2 UM

### 3.2.1 Model description

The UM is a seamless model in that it can be run at scales and resolutions from ~0.25° global runs to 10s of m limited area models. It is used operationally by the Met Office (who is the code owner) and other operation centers globally for weather forecasting and climate prediction. Some particular points to note regarding the model in general are:

- The UM uses semi-lagrangian dynamics which increases the usable timestep and reduces compute time (Wood et al., 2013).
- The UM includes the UK Chemistry and Aerosol Model (UKCA). UKCA an online chemistry model and is typically utilized for global simulations rather than limited domain operational runs (Morgenstern et al., 2009; O’Conner et al., 2014, www.ukca.ac.uk).
- For operational runs in the UK a separate model known as MURK is used which provides aerosol and visibility forecasts based on emissions within and near to the UK (Clark et al., 2008).
- As an alternative to either UKCA or MURK, aerosol concentrations may be defined by the climatology.
- Cloud condensation nuclei may be based upon either UKCA, MURK or climatological aerosol concentrations. Alternatively fixed specified numbers can be uses. These may be different over land and sea.
- The convection scheme within the UM has no cloud-aerosol interactions.
- The UM has options to use one of two cloud schemes for considering the fraction of a grid box covered by cloud; that of Smith (1990) or PC2 (Wilson et al., 2008).

### 3.2.2 Adaptations for DACCIWA

For the DACCIWA aircraft field campaign the UM was run with a resolution of 0.04° (~4.4 km) centered upon 3.5°E and 6°N with a size of 23° longitude and 20° latitude. The model uses a rotated grid such that the center of the domain is on the grid equator. The approximate domain is shown in Figure 3.2.1. This domain was chosen to include the potential aircraft ranges, the ground supersites, a significant fetch over the ocean from the SW (the source of the prevailing low level wind) and the nearby regions of common deep convection initiation (e.g. the mountainous regions of Nigeria).

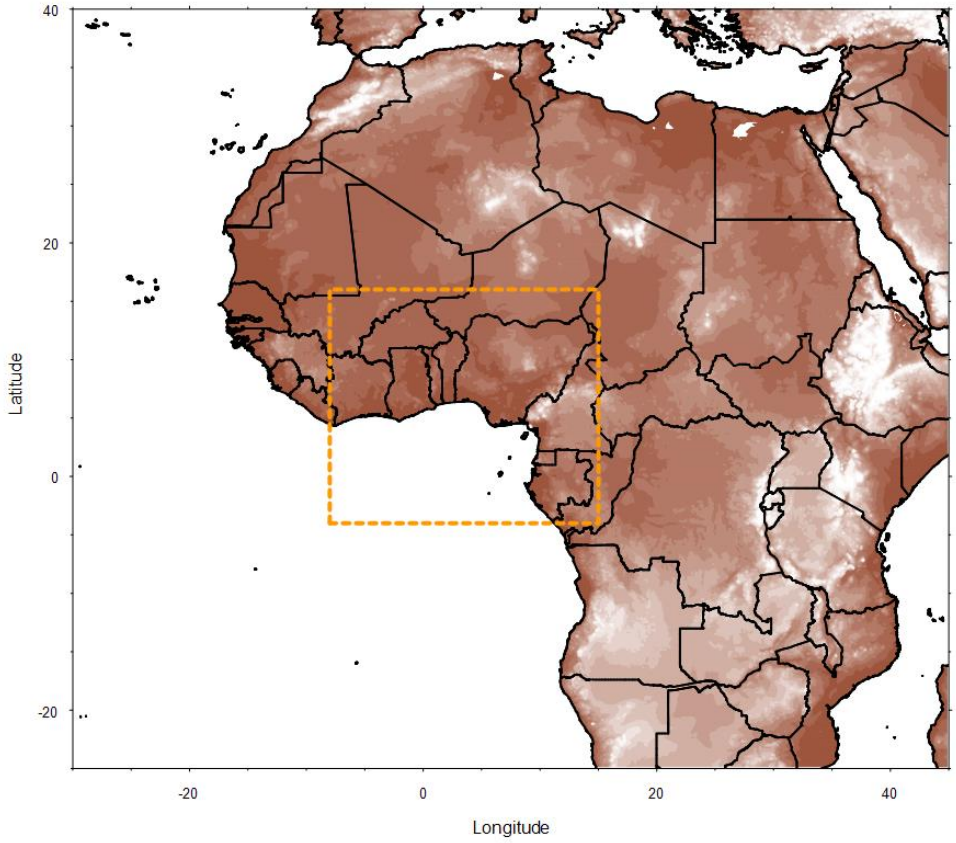


**Fig. 3.2.1** – Domain for the UM simulations (orange box).

The setup was similar to the operational forecast setup used for the UK by the Met Office, but with climatological aerosol. The convective parameterization was switched off so that resolved convection could develop. The warm rain process used was described by Khairoutdinov and Kogan (2000) and Boutle et al. (2014) and the Smith (1990) cloud scheme was used.

The model was initialized at 12 UTC every day and run for 72 hours providing a forecasting resource for the aircraft campaign. The first 12 hours of simulation was used for spin up of the unresolved features from the Met Office global analysis used for initialization. This period was therefore discarded. The UM will also be used for research within DACCIWA using a cloud microphysics model and aerosol model known as CASIM. CASIM allows the user to specify aerosol concentrations which affect the clouds but also has the potential to activate a feedback loop where clouds can modify the aerosol properties via wet deposition and in-cloud processing followed by release by evaporation. The runs described here did not use CASIM. Such runs are reserved for future work within DACCIWA.

### 3.2.3 Dataset analysis

The data presented here concentrates on the forecasts provided for the 36-50 hour after initialization, i.e. midnight to midnight two days after forecast initialization. This is because in general the forecast became available the morning after the simulation was run and tended to be used for planning flying activities for the day after. Therefore this period was the period generally used for forecasting.

The diurnal cycle of cloud fraction (Fig. 3.2.2) shows that the stratiform cloud in the 0-3 km region tends to have minimum spatial extent at 0 UTC. The coverage increases until 6 UTC when the peak coverage occurs at 1 km altitude. The cloud maximum then appears to descend in height to 0.6 km altitude by 9 UTC then rise again to 1 km by 12 UTC. The increase in altitude between 9 UTC and 12 UTC is likely to be due to convective mixing induced by solar heating of the surface during the day. The cause of the descent between 6 UTC and 9 UTC is not known at present. After 12 UTC the cloud amount decreases then grows again reaching a second minimum extent at 15 UTC and a second maximum at 21 UTC.

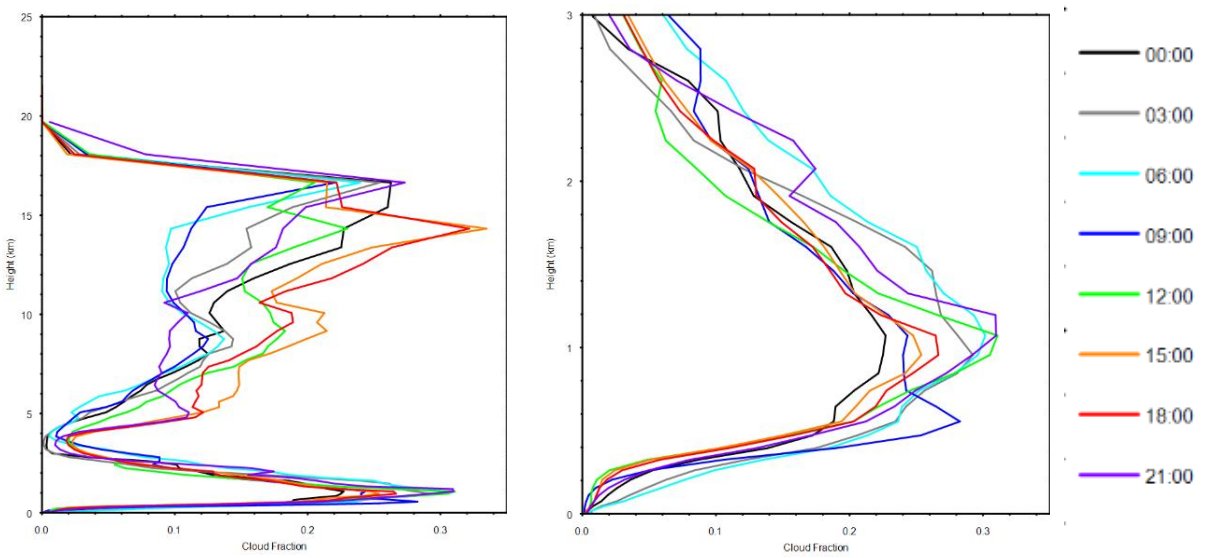


**Fig. 3.2.2** – Diurnal cycle of cloud coverage (between 0 and 0.34) profile, spatially averaged over Box 1 and temporally averaged from 27 June to 17 July 2016, in the altitude range 0-25 km (left) and 0-3 km (right). (D4)

The liquid water mixing ratio shown in Figure 3.2.3 follows a similar pattern to the cloud fraction, however the 21 UTC peak is larger than the 9 UTC peak. Given that the peaks in cloud fraction are similar, this implies that the clouds contain more liquid water in the evening.

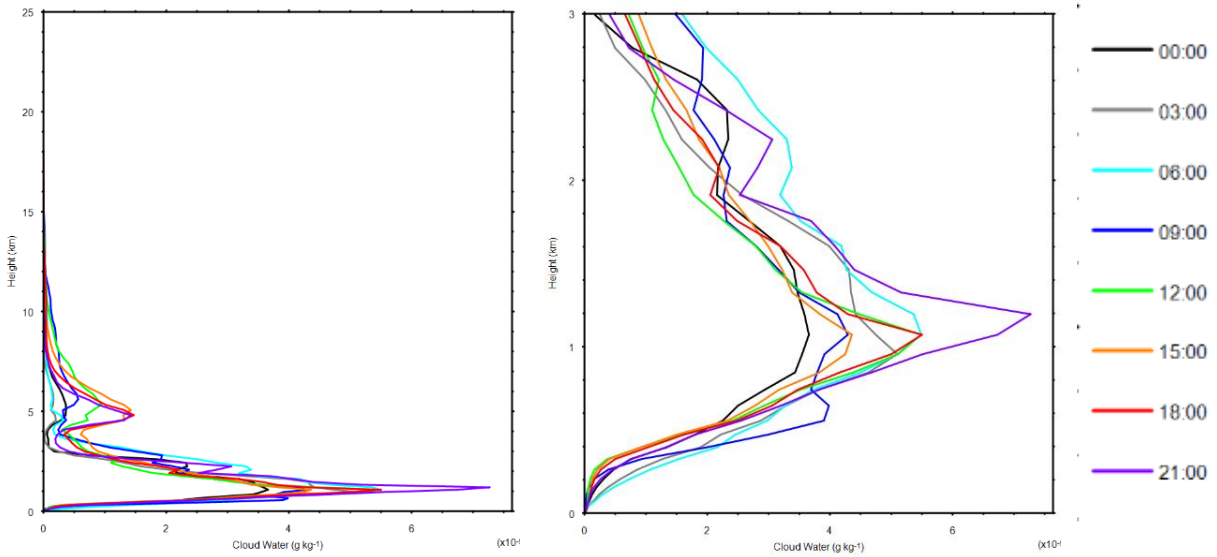


**Fig. 3.2.3** – As Fig.3.2.2 but for cloud liquid water (in $10^{-5}$ g $kg^{-1}$). (D4)

Figure 3.2.4a,b shows how the diurnal cycle of liquid water mixing ratio varies within one section over one day. Often within the stratiform cloud a thin layer of low liquid mixing ratio can be seen at approximately 1 km separating denser layers above and below. This may indicate a dynamical or air mass difference between the two layers. At 9 UTC the lower layer reaches its maximum extent, which matches the results of Figure 3.2.3. This layer then lifts between 9 UTC and 12 UTC then begins to deepen but dilute through the afternoon as deeper convection (diagnosed by vertical stripes in the liquid mixing ratio) occurs. By 21 UTC the system is dominated by 2-3 km deep cells and one very deep (10 km) cell has developed. This transition from stratiform cloud to cumuliform cloud is likely to be responsible for the initial dilution of cloud causing a minimum in the afternoon in Figures 3.2.2 and 3.2.3 followed by a maximum at 21 UTC although the details of the exact mechanisms involved require investigation.

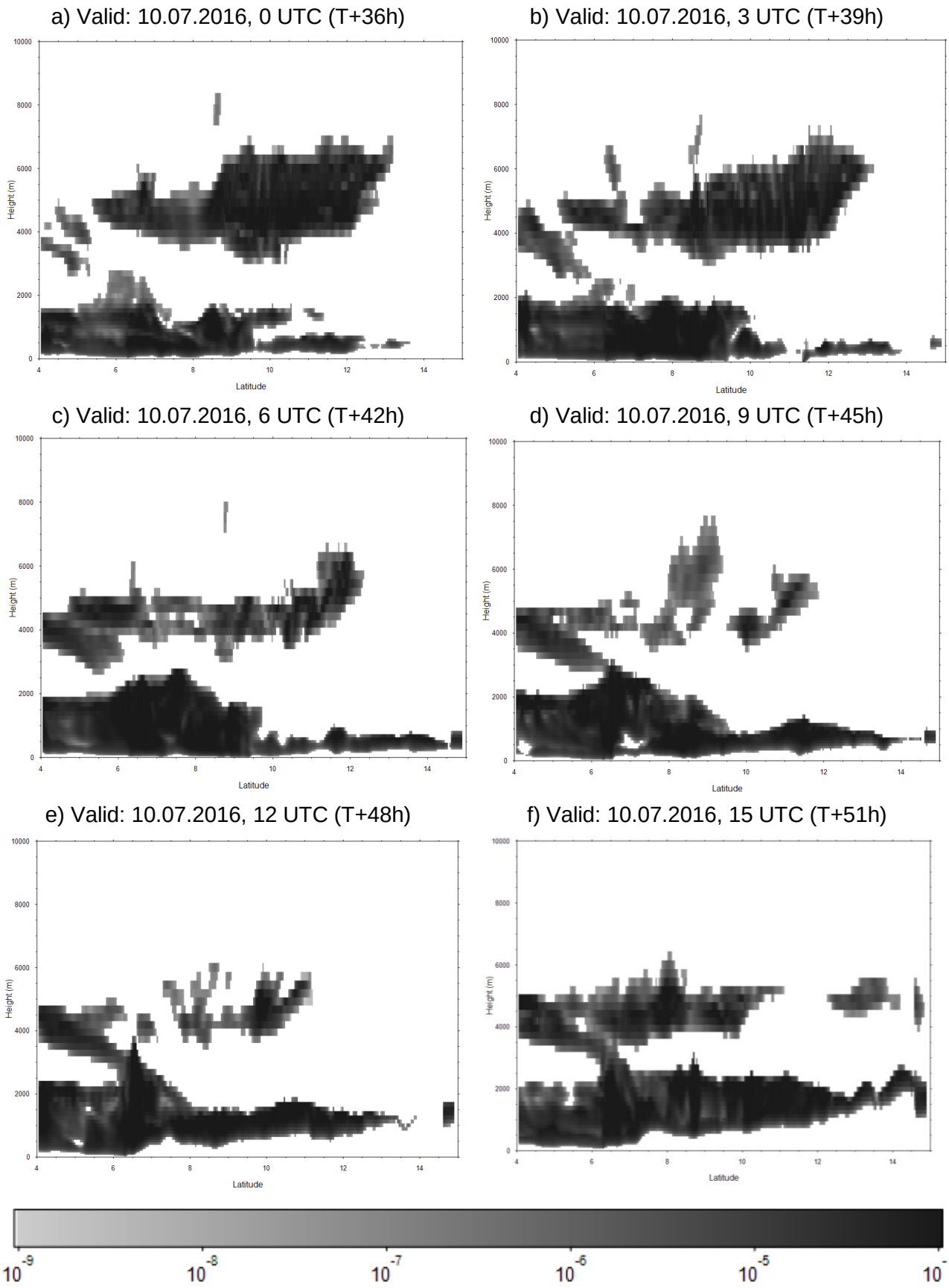


**Fig. 3.2.4a** - Diurnal cycle of liquid water mixing ratio (kg kg$^{-1}$) along a N-S section at 2°E (0-10km height) forecast for 10 July 2016 (0-15 UTC) with the run initialized at 12 UTC on 8 July 2016. (D4)

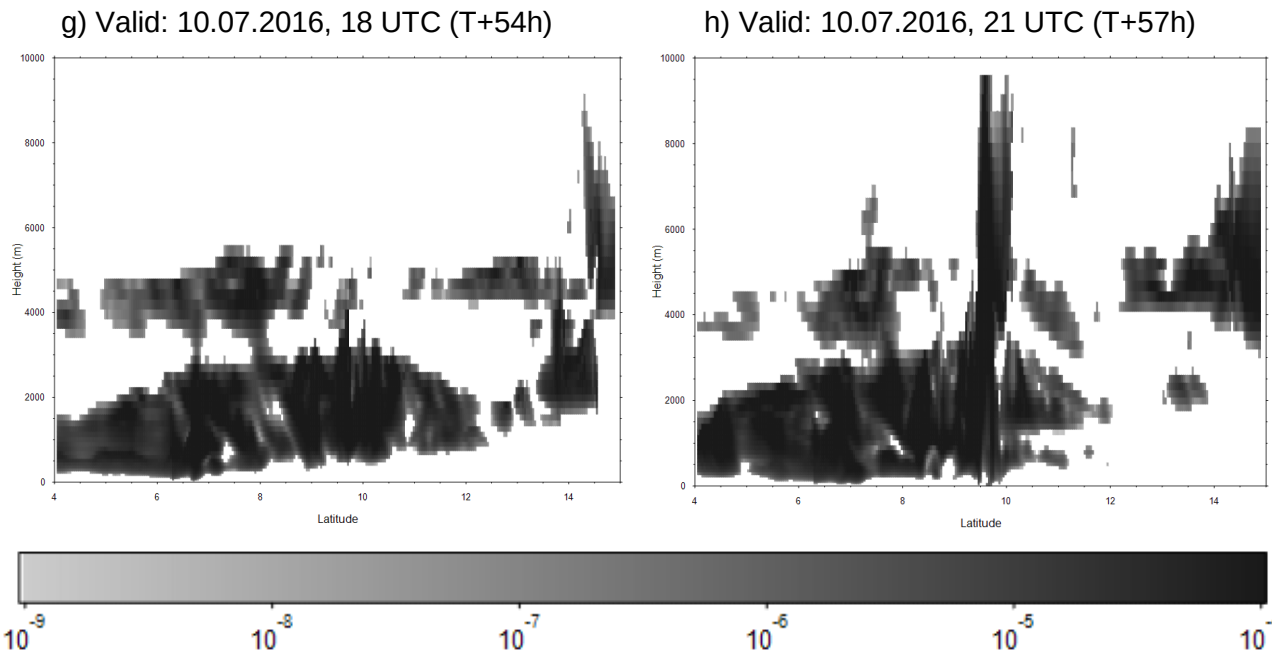


**Fig. 3.2.4b** - As Fig.3.2.4a but for 18-21 UTC. (D4)

The UM was also used during the aircraft field campaign to forecast deep convection. Figure 3.2.5 (left) shows the forecast output longwave radiation for the afternoon of 10 July 2016 (initialized at 8 July 2016, 0 UTC; T+52h). Deep convection is being initiated in central Nigeria and the Nigeria-Cameroon border. There is a propagating system that initialized earlier in the simulation on the north edge of the domain in Niger.

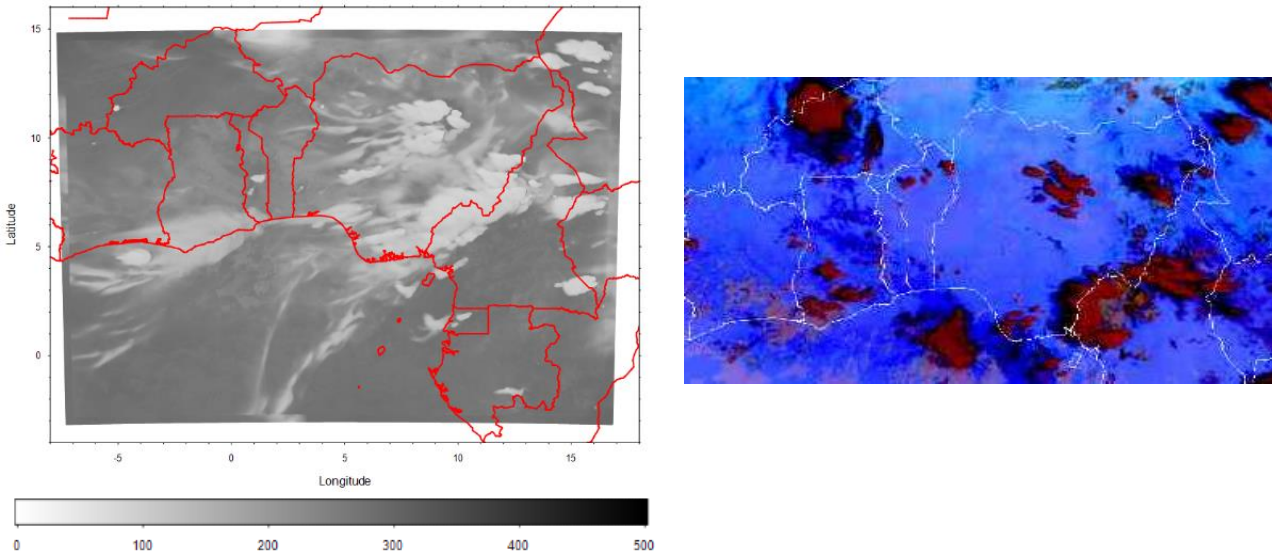


**Fig. 3.2.5** - Model outgoing top of atmosphere (TOA) longwave radiation (left, in W $m^{-2}$) for 8 July 2016, 16 UTC (D4). Deep convection and cirrus cloud is indicated by pale colours. SEVIRI false colour infrared observations (right) for 8 July 2016 17 UTC. Deep convection is indicated by red and black colours.

The SEVIRI satellite image (Fig. 3.2.5, right) shows deep convection initiating in similar locations and a propagating system in Niger. Although it should be noted that this observation is was obtained one hour later than the simulation. In general, the model regularly predicted initiation in this regions and at the Nigerian coast and these initiation point generally matched well with observations. The

model correctly predicted that these deep systems would propagate north of the aircraft measurement area throughout the field campaign.

### 3.2.4 Conclusion

The UM run at 4 km provided forecasts for the aircraft field campaign. In general it forecasts a stratiform cloud layer that expanded between 0 UTC and 9 UTC, lifted between 9 UTC and 12 UTC, changed to cumulus and diluted between 12 UTC and 18 UTC and had a second maximum in cloud coverage and liquid water mixing ratio at 21 UTC.

The forecasting of deep convective systems that may have impacted the flying operations was regarded as good with the initiation locations, propagation and timing of convection tending to match well with reality in the cases investigated.

## 3.3 CHIMERE

The main goal is to quantify the relative contribution of the pollutants due to biomass burning on the surface concentrations in urbanized areas. In order to take into account all important sources, a large area is modelled, encompassing the southern West Africa (Ivory Coast, Ghana, Benin, Nigeria) and representing all sites of interest for the DACCIWA project. Two simulations are carried out, with the same meteorology but one without fires emissions and one with. By difference between these two simulations, the relative contribution of combustion is quantified and discussed. The chemical composition of the aerosols is also presented.

### 3.3.1 Model description

For the simulations performed for this model evaluation, two regional models are used: (i) the WRF meteorological model calculates the meteorological variables and (ii) the CHIMERE chemistry-transport model calculates the field concentrations of gaseous and aerosols using the meteorological fields. For this first study, the models are used in off-line mode: WRF first simulates the dynamical fields and provide them as input for the transport to CHIMERE.

Two simulations domains are defined, DAW1 (red box in Fig. 1) and DWA2 (black box in Fig. 1). DWA1 and DWA2 have a constant horizontal resolution of 60x60 km and 20x20 km, respectively. The DWA2 domain is nested in the DWA1 domain both for meteorology and chemistry-transport. The largest domain, DWA1, is designed to take into account all sources in Africa (vegetation fires and mineral dust) emitting chemical species that can be transported over long distances. The smallest domain, DWA2, is designed to have an accurate horizontal resolution to well model the anthropogenic emissions and the land-sea gradients for the coastal sites. The modelled period ranges from 1 May to 29 July 2014.

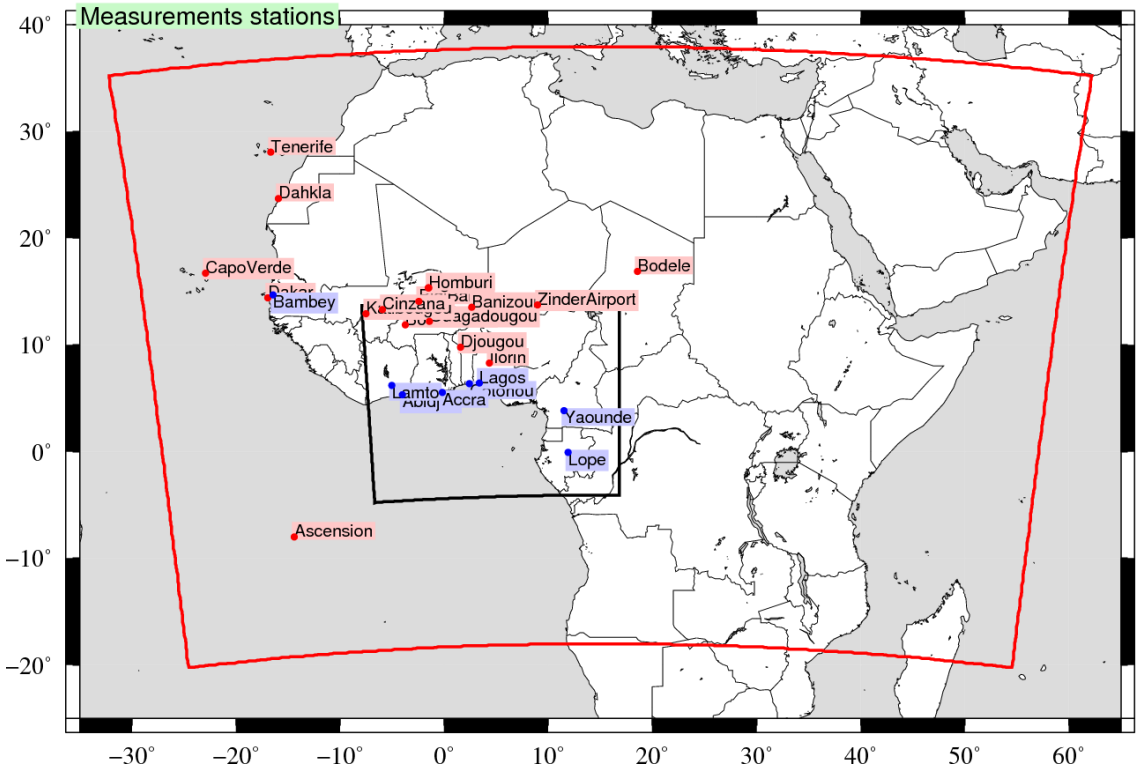


**Fig. 3.3.1** - The two simulation domains DWA1 (red) and DWA2 (black) for the WRF and CHIMERE models.

CHIMERE is a chemistry-transport model allowing the simulation of concentrations fields of gaseous and aerosols species at a regional scale. It is an off-line model, driven by pre-calculated meteorological fields. In this study, the version fully described in Menut et al. (2013a) and updated in Mailler et al. (2016) is used. If the simulation is performed with the same horizontal domain, the 28 vertical levels of the WRF simulations are projected onto 20 levels from the surface up to 200 hPa for CHIMERE. The chemical evolution of gaseous species is calculated using the MELCHIOR2 scheme. The photolysis rates are explicitly calculated using the FastJX radiation module (version 7.0b, Wild (2000); Bian (2002)). The modelled AOD is calculated by FastJX for the several wavelengths over the whole atmospheric column. At the boundaries of the domain, climatologies from global model simulations are used. In this study, outputs from LMDz-INCA (Hauglustaine et al., 2014) are used for all gaseous and aerosols species, except for mineral dust where the simulations from the GOCART model are used (Ginoux et al., 2001).

The anthropogenic emissions are issued from the HTAP global database (Janssens et al., 2015). Over the DWA1 domain, the main emissions are located at the north of the domain, the Mediterranean Sea (ships emissions) and the south of Europe. Along the African coast, the NO emissions generated by the ships are highlighted. The second major land source is clearly the urbanized areas of the Guinean Gulf. The vegetation fires emissions are quantified using the APIFLAME model described in Turquety et al. (2014) and used for example in Rea et al. (2015). These fluxes correspond to daily average values, constantly distributed in each hours of the day. Vertically, the surface fluxes are injected in the low troposphere and homogeneously in the boundary layer. The spatial extension of these emissions fires is mainly in Central Africa. The starting period for these fires is in April and the maximum of fluxes in the region are observed during July. The mineral dust emissions are calculated using the Alfaro and Gomes (2001) scheme, optimized following Menut et al. (2005b) and using the soil and surface databases presented in Menut et al. (2013b). To take into account the rain effect on mineral dust emissions limitation, a 'memory' function is added. During a precipitation event, the surface emissions fluxes are set to zero. After the

precipitation even, a smooth function is applied to account for a possible crust at the surface (and thus less emissions). The complete restart of emissions is obtained after 12h.

### 3.3.2 Adaptations for DACCIWA

The two models are used in their distributed versions without changes for DACCIWA.

### 3.3.3 Dataset analysis

During this monsoon period, large mesoscale convective systems are able to strongly impact the life cycle of gas and aerosols in the troposphere.

**Tab. 3.3.1** – Characteristics of the CHIMERE model datasets used for this study

| Characteristics | Dataset<br>D5 | D6 |
|---|---|---|
| Time period | 01.05.-29.07.2014 | 01.05.-29.07.2014 |
| Simulation domain | 25°W – 55°E,<br>20°S – 35°N | 8°W – 18°E,<br>5°S – 15°N |
| Grid mesh size (km) | 60 | 20 |
| Meteorological boundary conditions | WRF forced by NCEP global fields | WRF forced by WRF D5 in two-way nesting |
| Meteorological fields for (off-line) CHIMERE | WRF | WRF |
| Aerosol type (online/prescribed) | mineral dust (online),<br>sea salt (online),<br>biogenic (online),<br>vegetation fires (online) | mineral dust (online),<br>sea salt (online),<br>biogenic (online),<br>vegetation fires (online) |
| Aerosol treatment (bulk/modal/sectional) | sectional (10 bins) | sectional (10 bins) |
| Direct aerosol effect | no | no |
| Indirect aerosol effect | no | no |
| Chemical boundary conditions | LMDz-INCA | from D5 |
| Aerosol boundary conditions | LMDz-INCA (GOCART for mineral dust) | from D5 |
| Chemistry (online/prescribed, full chemistry) | online,<br>full chemistry | online,<br>full chemistry |

Over land, haboobs may induce sudden and intense mineral dust emissions. For this study, these systems are not the main focus, being localized more in the northern part of the studied region. Near

the coastline, various precipitating systems appear during this period of May to July, Fig. 3.3.2. This will constrain the transport of local emissions as well as the wet deposition of already emitted species.

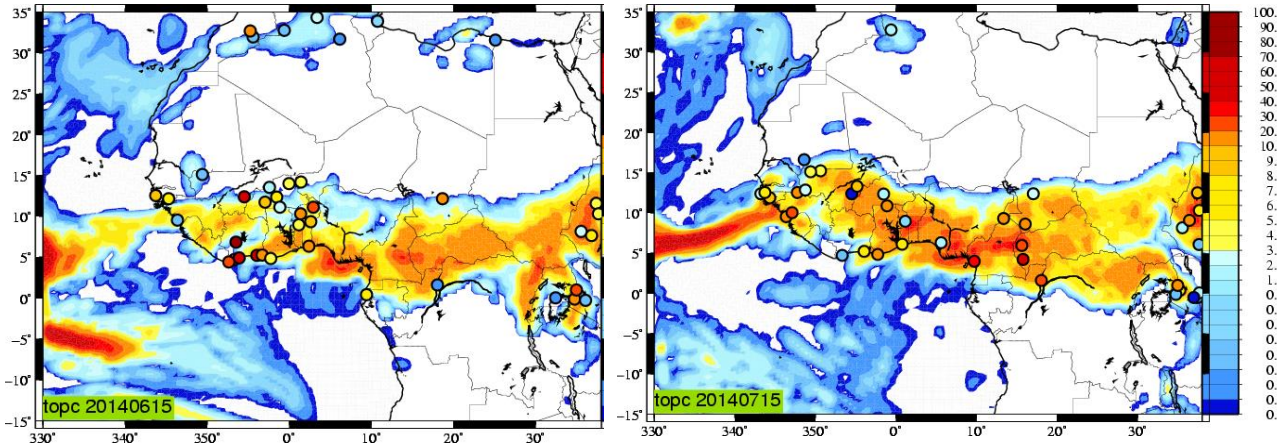


**Fig. 3.3.2** - Comparison between observed (BADC, circles) and modelled daily cumulated precipitation rate (mm/day) for the 15 June (left) and 15 July 2014 (right). For the precipitation measurements, only the non-zero daily cumulated values are reported on the plot. (D5 WRF)

The vegetation fires produce both gaseous and aerosol species. Among all species, the Particulate Organic Matter (POM) can be considered as a clear fire marker. In order to view the impact of the fires, this section presents vertical cross section of concentrations (Fig. 3.3.3). Knowing that the main transport pathway during this period is from East to West along the coast, an average of concentrations is done between the latitude 4°N to 7°N.
Results are presented for 15 June (no vegetation fires) and 15 July 2014 (with fires emissions). Without fires emissions, the POM concentrations are mainly due to surface anthropogenic emissions. This represents at the maximum 2 µg $m^{-3}$. With the fires emissions, the arrival of the biomass burning plume from the East is clear and the concentrations are significantly more important, ranging from 5 to 10 µg $m^{-3}$. The vertical extension is also important where concentrations greater than 10 µg $m^{-3}$ are modelled up to 4000 m.

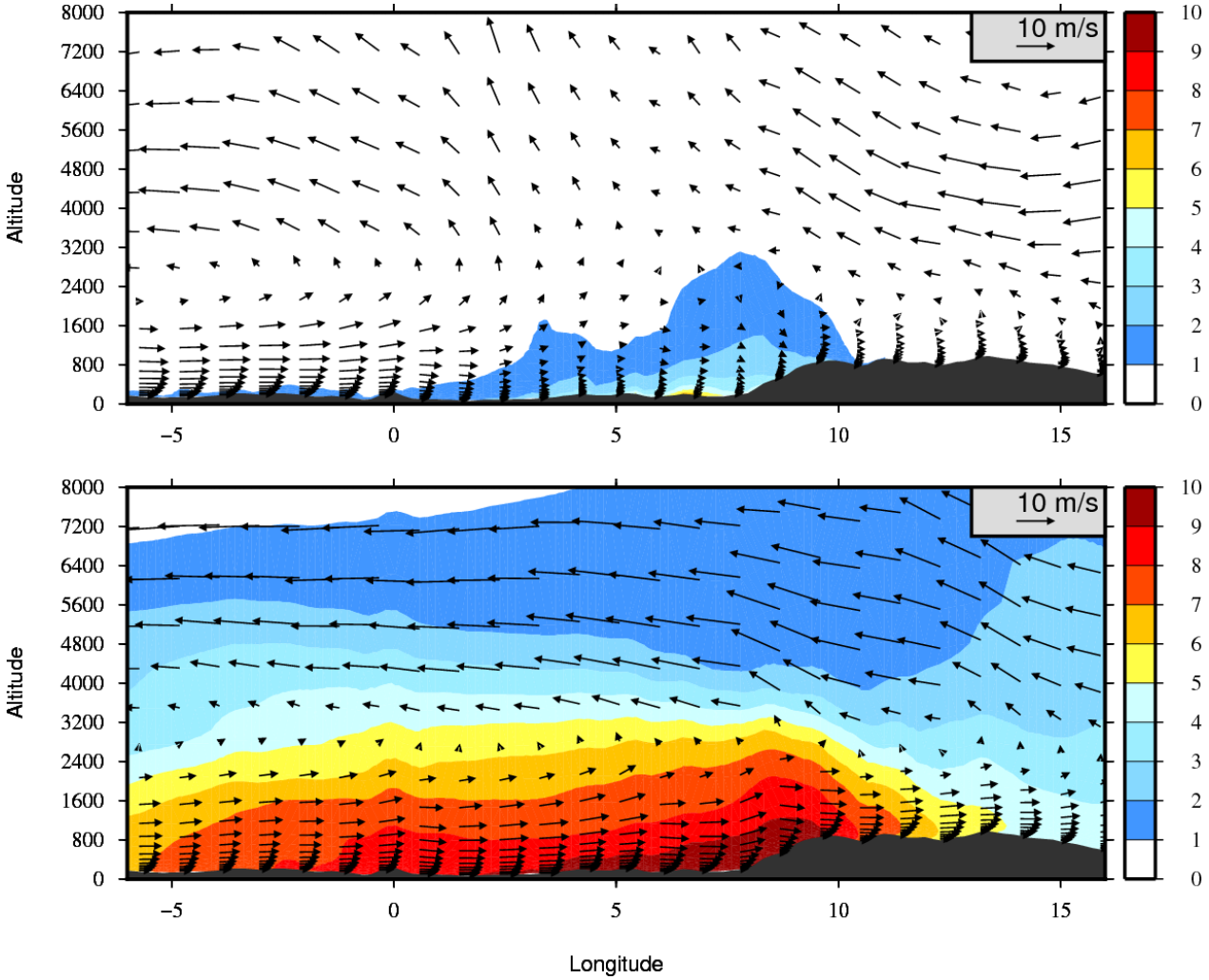


**Fig. 3.3.3** - Vertical cross-section (height in m) from 5°W to 15°E (as zonal average between 4°N and 7°N) of daily averaged POM (µg $m^{-3}$) concentrations for (top) 15 June 2014 with vegetation fire emissions and (bottom) 15 July 2015 without vegetation fire emissions. The black area corresponds to the topography. The wind vectors represent the zonal and vertical (x100) components. (D6)

For surface concentrations, we focus on the coastal urbanized areas. The analysis is done with the model only since there is no data available for the region and the studied period. Results are presented for Lagos (Nigeria) and Abidjan (Ivory Coast) (Fig. 3.3.4), representative of strongly urbanized coastal areas in the Guinea Gulf (see Fig. 3.3.1 for the location).

Two chemical species are presented: (i) ozone ($O_3$) - a secondary species, produced by anthropogenic, biogenic and fires emissions and (ii) carbon monoxide (CO) - a gaseous species, primarily emitted by anthropogenic and fires emissions. For ozone and carbon monoxide, there are no measurements available. Figure 3.3.4 presents time series of modelled surface concentrations, for the simulation without and with vegetation fires emissions. During the three months simulation, the concentrations increase continuously. This illustrates the slow long-range transport from Central Africa to these coastal urbanized sites.

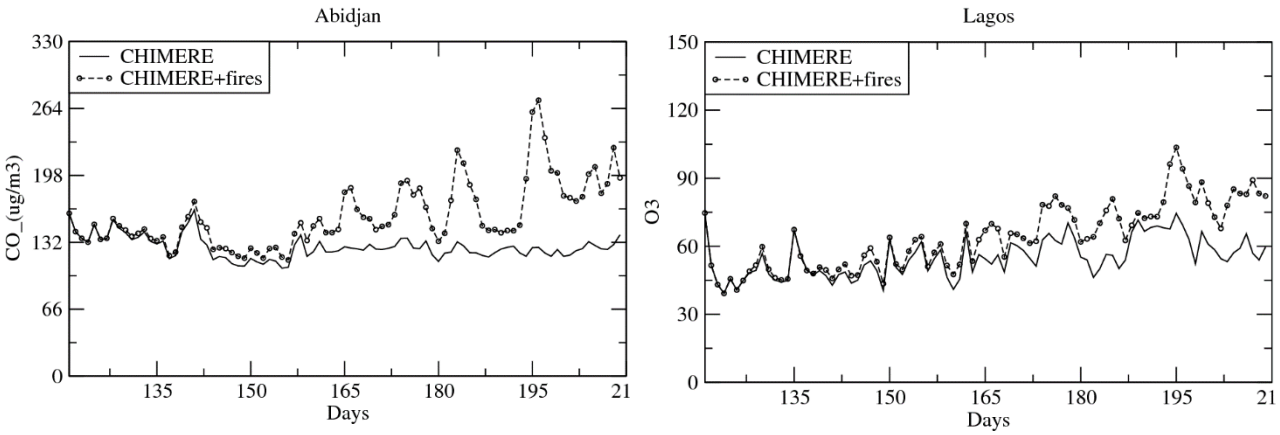


**Fig. 3.3.4** - Time series (1 May to 29 July 2014) of surface CO concentration (in µg $m^{-3}$) for Abidjan (left) and surface $O_3$ concentration (in ppbv) for Lagos (right) for the simulations with (dashed line) and without (solid line) vegetation fires emissions. See Fig. 3.3.1 for location of the cities Abidjan and Lagos. (D6)

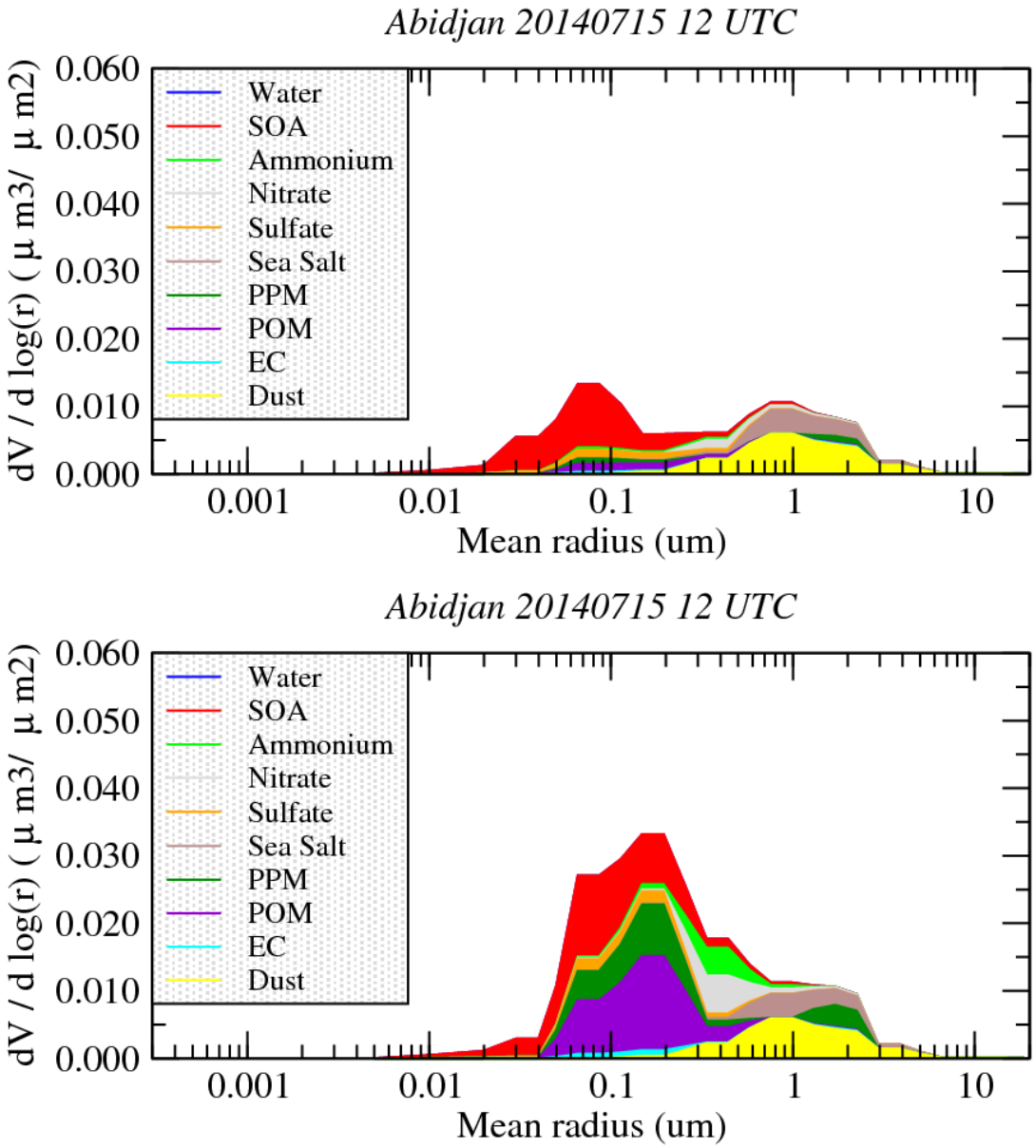


**Fig. 3.3.5** - Aerosol size distribution modelled at Abidjan for 15 July 2014 at 12 UTC for the simulation without (top) and with (bottom) vegetation fires. (D6)

Without fires, the most important contributions are due to the Secondary Organic Aerosol (SOA) for the fine mode (i.e. $D_p$<0.2 µm) and mineral dust for the coarse mode (i.e. $D_p$>1 µm). These relative contribution completely change for the case with fires emissions. The aerosol increase a lot in the fine mode, with important additional concentrations of PPM and POM. One can note also a non-negligible contribution of PPM in the coarse mode.

### 3.3.4 Conclusion

This study examines the atmospheric composition during the summer 2014 (from May to July) in the region of the Guinea Gulf. The main goal was to quantify the relative contribution of the vegetation fires emissions, occurring in Central Africa, on the aerosol surface concentrations in large urbanized areas such as Lagos and Abidjan.

The period was modeled with the meteorological model WRF and the chemistry-transport model CHIMERE with two nested domains: the largest one is designed to accurately estimate all sources around the Guinean Gulf and to provide realistic hourly boundary conditions to the nested one, centered on the urbanized areas. With this model configuration, two different simulations are performed, with and without vegetation fire emissions. By comparing the two simulations, this study analyzed and quantified the relative contribution of fires emissions on the AOD and PM10 surface concentrations budget.

The meteorological situation corresponds to a period favorable to convective events and monsoon. This year 2014 seems different than the others in general and shows a lot of rainfall than what is observed in general in this region. Compared to the BADC network measurements, it was shown that the WRF model simulates the most rainfall events, even if the model overestimates the frequency by simulating rainfall almost daily on the region.

The long-range transport of aerosol plumes was analyzed using data such as IASI for CO and AERONET and MODIS for AOD. This data was compared to two simulations, with and without fires. It was first shown that the Guinea Gulf coastal cities are not under the influence of mineral dust emissions, occurring more on the northern part of the region. The main atmospheric circulation during this period is with a main wind from south to north: the mineral dust being mostly emitted up to 10 degrees in latitude, there is no impact of these emissions on the surface concentrations in the urbanized areas close to the coastline.

On the other hand, it was shown that the vegetation fires in Central Africa represent an important increase for these urbanized areas in term of air pollution: both for gaseous ($O_3$ and CO) and aerosol (PM10), the vegetation fire emissions are responsible of an increase in concentrations from 10 to 100% (depending on the species and period). This large contribution appears during a summer where the precipitation rate is considered higher than for more 'typical' days. The effect is thus massive but could be more important during driest summers.

More precisely it has been shown that this increase is mainly constituted of Primary Particulate Matter (PPM) and Primary Organic Matter (POM). These relative contributions are mainly in the fine mode for PPM and POM, but a non-negligible contribution was also modelled in the aerosol coarse mode for PPM.

This study shows that the understanding of atmospheric pollution for urbanized areas in the Guinean Gulf region must take into account the vegetation fires, even if they seem located far from this region. In this study, the model configuration was off-line and this may induce a bias in the result: the direct effect of dense biomass burning plumes may affect directly the convection in the region and the large amount of aerosols may also change the precipitation by indirect effect. The next step will be to study this interaction by using an on-line coupled modeling system.

## 3.4 ECHAM-HAM

### 3.4.1 Model description

The aerosol module HAM was first implemented in the 5th generation of the atmospheric general circulation model ECHAM (ECHAM5, Roeckner et al., 2003) by the Max Planck Institute for Meteorology (MPI-M) and a first comprehensive description is provided in Stier et al (2005). Over the past years, the HAM module has been improved and complemented with new processes (now it is called HAM2) as described in Zhang et al. (2012). Also ECHAM underwent substantial developments and improvements during the recent years. The 6th generation of the ECHAM family has been developed (Stevens et al, 2013).

ECHAM6 employs a spectral transform dynamical core and a flux-form semi-Lagrangian tracer transport algorithm from Lin and Rood (1996). Vertical mixing occurs through turbulent mixing, moist convection (including shallow, deep, and mid-level convection), and momentum transport by gravity waves arising from boundary effects or atmospheric disturbances. Sub-grid scale cloudiness (stratiform clouds) is represented using the scheme of Sundqvist (1989) which calculates diagnostically the grid cell cloud fraction as a function of the relative humidity in the given grid cell, once a threshold value is exceeded. Liquid (cloud water) and solid (ice water) condensates are treated prognostically following Lohmann and Roeckner (1996). In ECHAM6- HAM, additional prognostic equation for the numbers concentrations of cloud droplets and ice crystal are included. Radiative transfer in ECHAM6 is represented using the radiation transfer broadband model (RRTMG), which considers 16 and 14 bands for the shortwave (820 to 50000 cm-1) and longwave (10 to 3000 cm-1) parts of the spectrum, respectively (Iacono et al., 2008).

Radiative transfer is computed based on compounds present in the atmosphere and their related optical properties. Trace gas concentrations of long-lived greenhouse gases are specified in the model (except for water vapor). Optical properties of clouds are calculated for each band of the RRTMG scheme using Mie theory and the concentration of liquid water and ice condensates as computed by the 1-moment or 2-moment scheme in ECHAM6 and ECHAM6-HAM2 models, respectively.

Aerosol microphysics is simulated using the M7 module (Vignati et al., 2004), which accounts for sulfate, black carbon, particulate organic matter, sea salt, and dust. The atmospheric aerosol population is described as a superposition of seven lognormal distributed modes for which standard deviations are prescribed. The total number concentration and masses of the different chemical components are prognostic variables in the model. The modes are divided into soluble, internally mixed modes (containing sulfate) and insoluble, externally mixed modes, which are assigned to different size ranges. The modal diameters can vary and are calculated at each time step from the mass and number concentrations for each mode. Dust particles are considered as part of the soluble and insoluble accumulation and coarse modes. Sedimentation and dry and wet deposition are parameterized as functions of the aerosol size distribution, composition, and mixing state and depend on the ECHAM6 meteorology. The emission fluxes of dust, sea salt, and dimethyl sulfide from the oceans (DMS) are calculated online, based on the model meteorology. Anthropogenic emissions are prescribed.

### 3.4.2 Adaptations for DACCIWA

After a brief evaluation of first test simulations we decided to use the ECHAM6.3-HAM2.3 version in the framework of the DACCIWA project. We apply different emission inventories for anthropogenic aerosols. So far we used the ACCMIP (Atmospheric Chemistry and Climate Model Intercomparison Project) emission inventory (Lamarque et al., 2010), ACCMIP + GFAS (Global Fire Assimilation System) (Heil et al., 2010) for biomass burning and the HTAPv2.0 emission inventories. We also plan to use the emission inventory developed in WP2 of the DACCIWA project for model simulations.

### 3.4.3 Dataset analysis

To evaluate our aerosol model HAM2.3 we performed a set of nudged simulations. In the following we present results of simulations using (i) the ACCMIP emission inventory (D8), (ii) the ACCMIP emission inventory but GFAS for biomass burning aerosol (D7, emissions are multiplied by 3.4) (see Tab. 3.4.1). The large-scale dynamics is nudged to ERA-Interim reanalysis. The focus is on the year 2008.

**Tab. 3.4.1** - Performed simulations with ECHAM6.3-HAM2.3

| Characteristics | Dataset D7 | D8 | D9 | D10 | D11[1] |
|---|---|---|---|---|---|
| Time period | 2000-2010 | 2000-2010 | 1996-2010 | 1996-2010 | 1996-2010 |
| Simulation domain | global | global | global | global | global |
| Grid mesh size (km) | 200 (T63) | 200 (T63) | 200 (T63) | 200 (T63) | 200 (T63) |
| Convection parameterization | yes | yes | yes | yes | yes |
| Meteorology | prescribed with ERA-Interim | prescribed with ERA-Interim | online calculated (AMIP SST, SIC) | online calculated (AMIP SST, SIC) | online calculated (AMIP SST, SIC) |
| Cloud microphysics | two-moment | two-moment | two-moment | two-moment | one-moment |
| Aerosol type (online/prescribed) | mineral dust, sea salt and DMS: online; anthrop.: prescribed | mineral dust, sea salt and DMS: online; anthrop.: prescribed | mineral dust, sea salt and DMS: online; anthrop.: prescribed | mineral dust, sea salt and DMS: online; anthrop.: prescribed | mineral dust, sea salt and DMS: online; anthrop.: prescribed |
| Aerosol treatment (bulk/modal/sectional) | modal | modal | modal | modal | bulk |
| Direct aerosol effect | yes | yes | yes | yes | climatology |
| Indirect aerosol effect | yes | yes | yes | yes | climatology |
| Nudging | yes | yes | no | no | no |
| Emission inventory | ACCMIP and GFAS[2] | ACCMIP | ACCMIP and GFAS[2] | ACCMIP | no |

[1] ECHAM6.3 without HAM2.3

[2] GFAS for biomass burning aerosols

In Simulation D8 with use of the ACCMIP emission inventory for both anthropogenic and biomass burning aerosols, a 10 year average of 7.3 Tg/yr BC, 61.4 TG/yr OC, 5.1 + 221 Tg/yr $SO_4$, 1094 Tg/yr Dust, and 5713 Tg/yr Sea salt particles are emitted (Table 3.4.2). These values are comparable

with estimates based on global aerosol-climate models or observations. The calculated lifetimes of BC (6.8 d), OC (5.9 D), SO4 (4.7 d), Dust (5.6 d), and Sea salt (0.7 d) are reasonable.

**Tab. 3.4.2** - Global budget for D8

| | **Black carbon (BC)** | **Organic carbon (OC)** | **Sulfate ($SO_4$)** | **Mineral dust (DU)** | **Sea salt (SEAS)** |
|---|---|---|---|---|---|
| Emission (in Tg $y^{-1}$) | 7.3 | 61.4 | 5.1 + 221[1] | 1094 | 5713 |
| Burden (in Tg) | 0.14 | 1.0 | 2.9 | 17.06 | 11.18 |
| Deposition (in Tg $y^{-1}$) | 7.4 | 61.8 | 226.6 | 1110 | 5725 |
| Lifetime (in d) | 6.78 | 5.91 | 4.69 | 5.62 | 0.71 |

[1] emission + production

A map of the 10-year averaged aerosol optical thickness (AOT) at 675 nm as simulated by simulation D7 and D8 and measured at AERONET stations is shown in Figure 3.4.1. In Africa, both simulations capture the measurements quite well. With use of the GFAS emissions for biomass burning aerosols (simulation D7) the AOT is overestimated in Ascension Island. This could indicate that the biomass burning emissions are overestimated in the GFAS inventory. This goes with the findings of the comparison between modelled AOT at 675 nm and satellite measurements (NRL aqua). In Figure 3.4.3 the time series for a regional averaged AOT in Sahara (top) and the tropical Savannah in Africa (bottom) are shown. In tropical Savannah the AOT is overestimated in simulation D7 during summer. For the Sahara region the simulations reproduce the AERONET (Fig. 3.4.2) and the NRL aqua estimates reasonable. In comparison to the satellite estimates the model seems to overestimate the AOT during spring, but it seems to underestimate the AOT at AERONET sites during fall.

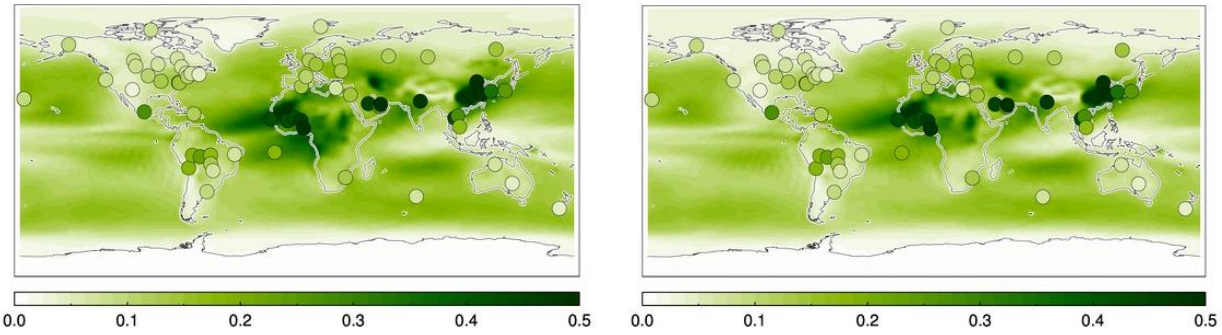


**Fig. 3.4.1** - AOT at 675 nm as simulated by D7 (nudged ACCMIP+GFAS, left) and D8 (nudged ACCMIP, right). The circles represent measurements of AERONET stations. The datasets are collocated (figure provided by N. Schutgens).

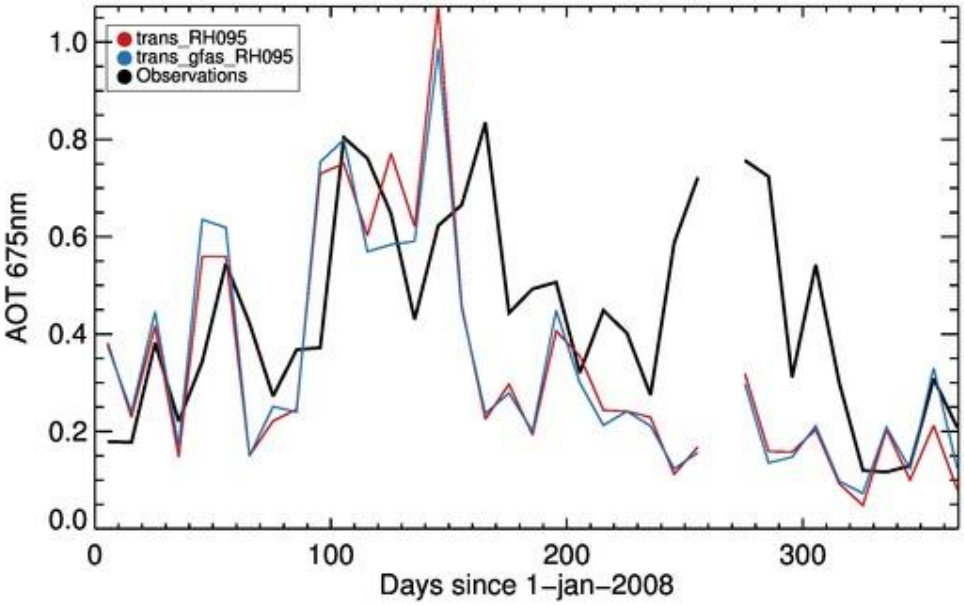


**Fig. 3.4.2** – Time series of AOT at 675nm as measured by AERONET stations (black) and simulated by D7 (blue) and D8 (red) averaged about the Sahara for 2008. The datasets are collocated (figure provided by N. Schutgens).

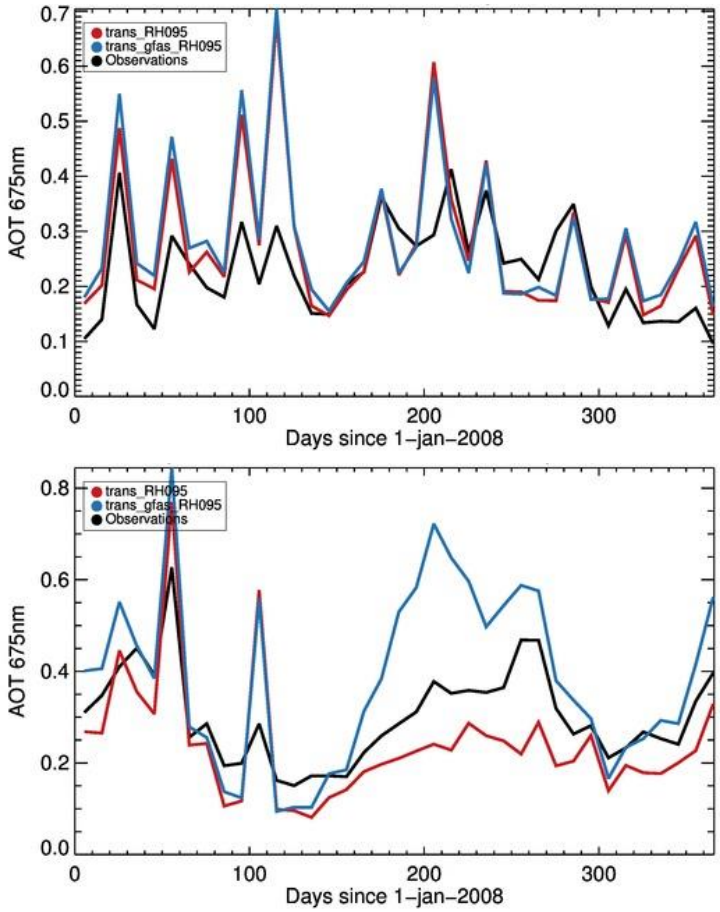


**Fig. 3.4.3** – Time series of AOT at 675nm as measured by NRL aqua (black) and simulated by D7 (blue) and D8 (red) averaged about the Sahara (top) and the tropical savannah in Africa (bottom) for 2008. The datasets are collocated (figure provided by N. Schutgens).

In the framework of the AMMA (African Monsoon Multidisciplinary Analyses) project, aircraft measurements of OC (Fig. 3.4.4 left) and $SO_4$ (Fig. 3.4.4 right) were performed in July/August 2006. The model seems to underestimate the OC concentrations but since the error estimates of the measurements are quite large, the simulated concentrations are still within the uncertainty range. But our model clearly overestimates the $SO_4$ concentration in low altitudes.

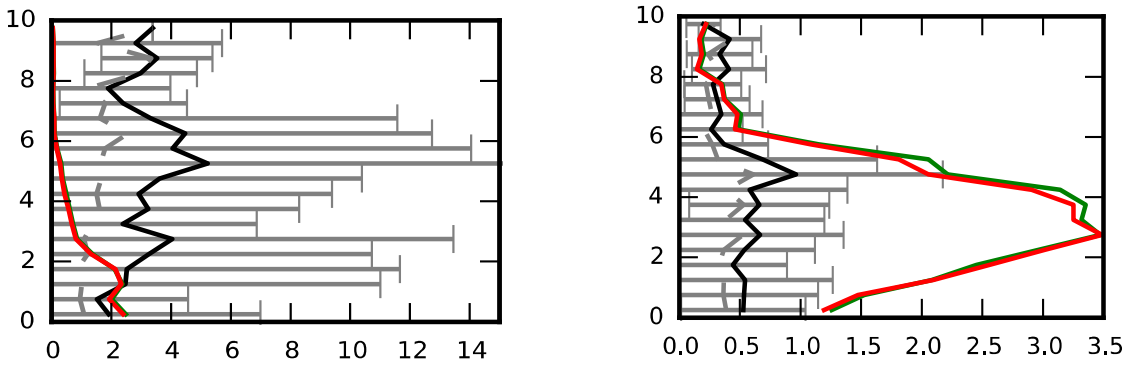


**Fig. 3.4.4** - Vertical profile (height in km) of OC (left) and $SO_4$ concentrations (in µg/m$^3$) as measured during the AMMA (African Monsoon Multidisciplinary Analyses) aircraft campaign (black) and simulated by D8 (red). Data are provided by Heald et al. (2011).

The evaluation of the capability of ECHAM6 and ECHAM6-HAM2 to reproduce the West African monsoon system is mainly done in the framework of work package 7 of the DACCIWA project. But since the ability of the model system to reproduce the African climate is essential to simulate the aerosol distribution (especially in the future, when it is not possible to prescribe the large scale circulation with observations) and the aerosol-cloud interactions, we will summarize our findings here. For this purpose, we performed free (not nudged) simulations (D9-D11, for details see table 3.4.1), the sea surface temperature (SST) and sea ice cover (SIC) is prescribed from AMIP2.
A zonal average between 10°W and 10°E of the 2 m temperature and precipitation is shown in Figure 3.4.5. The 2m temperature is overestimated in the ECHAM6 simulation (D11, blue line in Fig. 3.4.5). In particular, the simulated 2m temperature is too high north of 10°N. The simulated 2m temperature is lower when considering the online calculated aerosol distribution (simulations D9 and D10 with ECHAM6-HAM2, green and red lines). Using the ACCMIP emission inventory for both, anthropogenic and biomass burning aerosols, the 2m temperature is lowest although the biomass burning aerosol emissions are lower. But due to feedbacks between the aerosols and the climate, the wind velocity increases in simulation D10. Therefore, the emission fluxes of sea salt and dust particles increase.
In Northern Hemispheric summer the precipitation band is located between 0° and 18°N. All our simulations capture this. But the amount of precipitating water is underestimated south of 10°N in all our simulations.

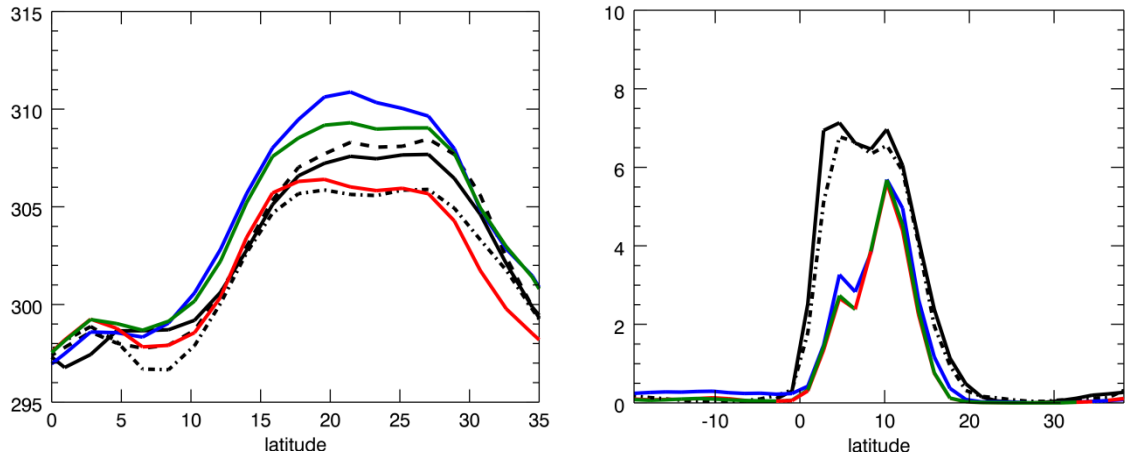


**Fig. 3.4.5** - Zonal mean of 2m temperature (0°-35°N, in K) (left) and precipitation (20°S-40°N, in mm/d) (right) for June-July-August averaged over 15 years (1996-2010). Reanalysis are shown in black (temperature: CRU (solid line), ERA-Interim (large dashed line), NCEP (dashed line); precipitation: CRU (solid line) and CMAP (dashed line)), simulation D11 (free ECHAM6.3) in blue, D10 (free ACCMIP) in red and D9 (free ACCMIP+GFAS) in green.

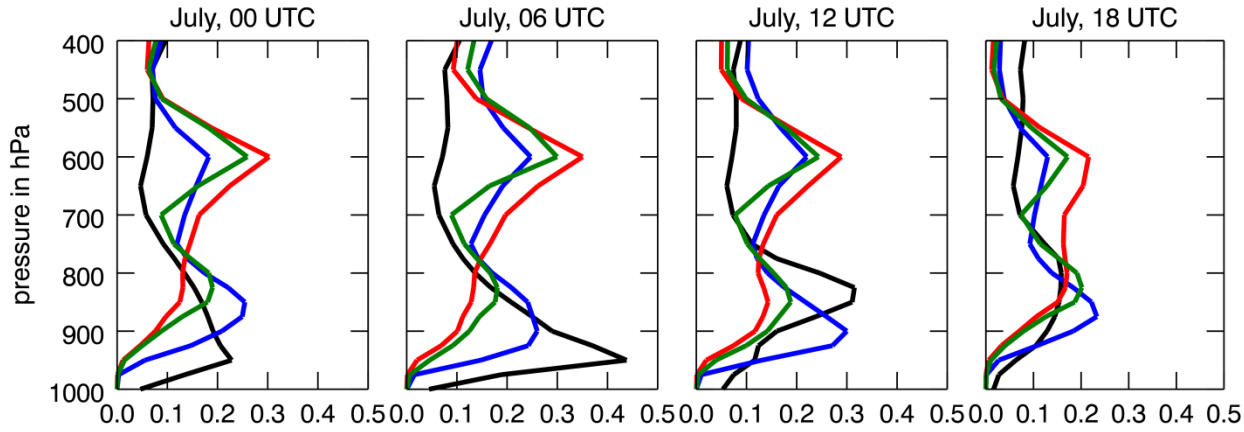


**Fig. 3.4.6** - Vertical profile of cloud cover as analysed by ERA-Interim (black) and simulated by D11 (blue), D10 (red), and D9 (green). The profiles are spatially averaged over Box 1 and temporally averaged over 15 years (1996-2010).

The vertical profile of total cloud cover in our region of interest (Box 1) is shown in Figure 3.4.6. The pure climate model is able to reproduce the low level clouds. But the distinct diurnal cycle is not captured by ECHAM6. During the night the cloud cover is underestimated and the clouds are located in too high altitudes.

The coupled model almost fails in reproducing the low level clouds. Only the simulation using the GFAS emission inventory produces low level clouds, but they are located in too high altitudes. The difference between the coupled simulations is in the cloud droplet number concentration at low altitudes, which is higher in the simulation using the GFAS emission inventory (D9) than in the one using the ACCMIP inventory for all aerosols (D10, Figure 3.4.7).

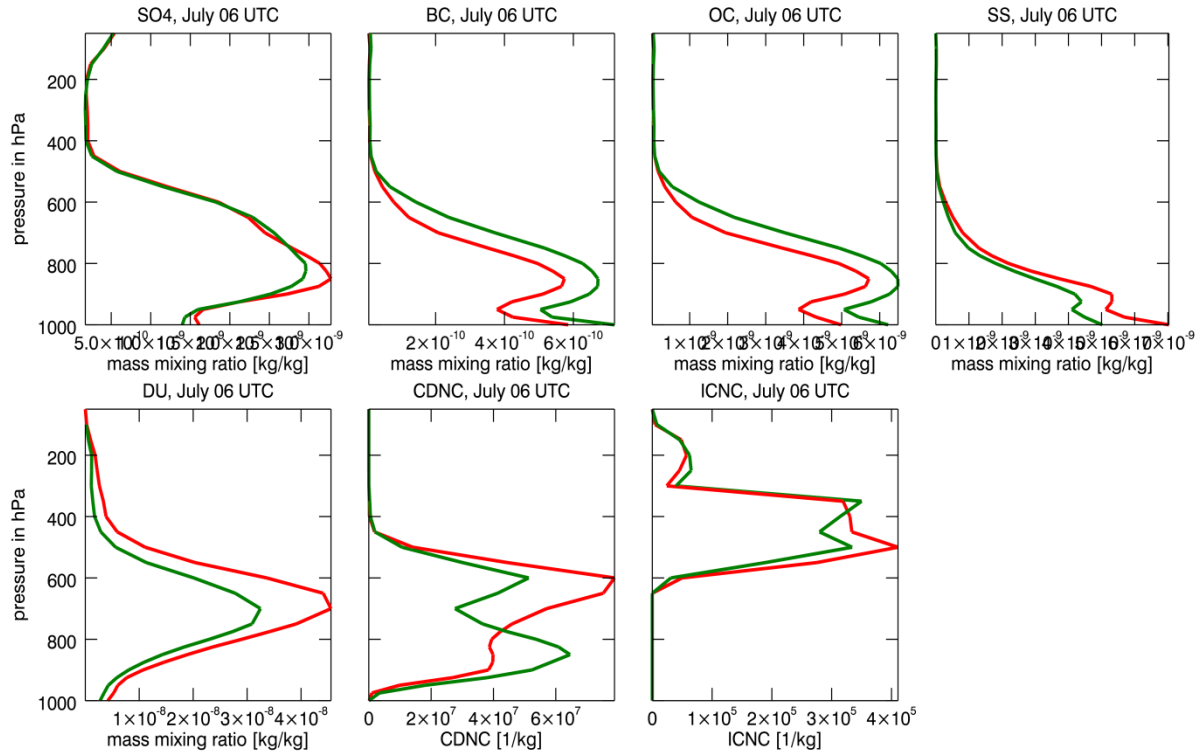


**Fig 3.4.7** - Vertical profile of mass mixing ratio (in kg/kg) of SO4, BC, OC, SEAS (from top left to right) and DU (bottom left) as well as the number concentration in ($kg^{-1}$) of cloud droplets (CDNC) and ice particles (ICNC) (bottom middle and right respectively) as simulated by D10 (red) and D9 (green). The profiles are spatially averaged over Box 1 and temporally averaged over 15 years (1996-2010).

### 3.4.4 Conclusion

The global aerosol climate model ECHAM6-HAM2 was evaluated in terms of its ability to represent the aerosol distribution in West Africa. For this purpose, we performed two nudged simulations, whereby the large scale circulation was prescribed by ERA-Interim reanalysis. To simulate the anthropogenic and biomass burning aerosol emissions we used emission inventories, first the ACCMIP inventory, second the ACCMIP plus GFAS inventory for biomass burning aerosol emissions. In summary the AOT is reproduced reasonable in the model, but the OC concentrations seem to be underestimated and the $SO_4$ concentrations seem to be overestimated during summer times. A comparison of simulated and satellite derived AOT in tropical Savanna indicates that the biomass burning emissions could be overestimated with use of the GFAS inventory.

We will discuss the interactions between aerosol and clouds in WP4. ECHAM6-HAM2 considers both, the direct and indirect aerosol effects. The basis for the future analysis is the ability of the model to represent the African Monsoon system realistically. For testing that ability of our model system we performed three not nudged simulations, one with use of the pure climate model ECHAM6, here the aerosol distribution for the consideration of the direct and indirect aerosol effects is prescribed. The other two simulations were performed with the aerosol climate model ECHAM6-HAM2 with full interactions between aerosols and climate; again we used the ACCMIP and the ACCMIP plus GFAS emission inventories.

The N-S section of the 2m temperature is reproduced well by the coupled model. All simulations are able to simulate the latitudinal depended location of the rain, but they underestimate the amount of rain south of 10°N. This has to be taken in mind when performing the future projections.

The pure climate model simulates the presence of low level clouds at the Guinea Coast. But it does not reproduce their diurnal cycle. The coupled aerosol-climate model underestimates the presence of low level clouds. With use of the GFAS emission inventory the cloud droplet number concentration is higher in low altitudes and some low level clouds are formed.

In the framework of the DACCIWA project we integrated the ability to output tendencies (temperature and specific humidity) into the model. Together with WP7 we will analyze the output tendencies. Further we will expand our set of ECHAM6-HAM2 AMIP simulations. We prepare the model for the use of the HTAPv2 emission inventory, as well as the inventory developed in DACCIWA WP2 for West Africa.

## 3.5 IFS-CAMS

### 3.5.1 Model description

The Composition-Integrated Forecast System is an extended version of the Integrated Forecast System (IFS) with capabilities for modelling and assimilation of atmospheric constituents such as gases and aerosols. It is run operationally within the Copernicus Atmosphere Monitoring Service (CAMS). The composition modules are online within IFS, offering a comprehensive description of the state of the atmosphere. In this section we focus in particular on the aerosol modules within C-IFS. Note that the CAMS forecasts have been used operationally during the aircraft campaign. Specific runs with the system to understand the importance of aerosols in the DACCIWA region have been also performed. These will be described below in the section related to the results.

Aerosol models range from very basic to very complicated schemes and the correct balance between needed sophistication and available computing resources needs to be found. CAMS currently uses a simple bin scheme for its near-real-time forecasts and the reanalysis (IFS-LMD), while implementing a more elaborate modal scheme for the future (IFS-GLOMAP, Mann et al. 2010).

The IFS-LMD aerosol scheme is the scheme that was introduced to add aerosol modelling to the ECMWF IFS forecasting system. It is currently used for the daily analysis and 5-day forecast and was also used for the Monitoring Atmospheric Composition and Climate (MACC) reanalysis.

The initial package of ECMWF physical parameterizations dedicated to aerosol processes mainly follows the aerosol treatment in the LOA/LMD-Z model (Boucher et al. 2002; Reddy et al. 2005). Five types of tropospheric aerosols are considered: sea salt, dust, organic and black carbon, and sulphate aerosols. Prognostic aerosols of natural origin, such as mineral dust and sea salt are described using three size bins. For dust, radius bin limits are at 0.03, 0.55, 0.9, and 20 microns while for sea-salt radius bin limits are at 0.03, 0.5, 5 and 20 microns. Please note, that currently the sea salt is provided at 80% relative humidity. This means that the bins and mixing ratios are not defined in terms of dry matter. To get back to dry matter a reduction factor of 4.3 is needed for the mass mixing ratios and a reduction factor of 1.99 for the radii. Emissions of dust depend on the 10-m wind, soil moisture, the UV-visible component of the surface albedo and the fraction of land covered by vegetation when the surface is snow-free. A correction to the 10-m wind to account for gustiness is also included (Morcrette et al. 2008). Sea-salt emissions are diagnosed using a source function based on work by Guelle et al. (2001) and Schulz et al. (2004). In this formulation, wet sea-salt mass fluxes at 80% relative humidity are integrated for the three size bins, merging work by Monahan et al. (1986) and Smith and Harrison (1998) between 2 and 4 µm. Sources for the other aerosol types which are linked to emissions from domestic, industrial, power generation, transport and shipping activities, are taken from the SPEW (Speciated Particulate Emission Wizard), and EDGAR (Emission Database for Global Atmospheric Research) annual- or monthly-mean climatologies. More details on the sources of these aerosols are given in Dentener et al. (2006). Emissions of OM, BC and SO2 linked to fire emissions are obtained using the GFAS system based on MODIS satellite observations of fire radiative power, as described in Kaiser et al. (2011). Several types of removal processes are considered: dry deposition including the turbulent transfer to the surface, gravitational settling, and wet deposition including rainout by large-scale and convective precipitation and washout of aerosol particles in and below the clouds. The wet and dry deposition schemes are standard, whereas the sedimentation of aerosols follows closely what was introduced by Tompkins (2005) for the sedimentation of ice particles. Hygroscopic effects are also considered

for organic matter and black carbon aerosols. A detailed description of the ECMWF forecast and analysis model including aerosol processes is given in Morcrette et al. (2009) and Benedetti et al. (2009). An in-depth evaluation is presented in Mangold et al. 2010.
MODIS AOD data at 550 nm are routinely assimilated in a 4D-Var framework which has been extended to include aerosol total mixing ratio as extra control variable (Benedetti et al. 2009). A variational bias correction for MODIS AOD is implemented based on the operational set-up for assimilated radiances following the developments by Dee and Uppala (2008). The bias model for the MODIS data consists of a global constant that is adjusted variationally in the minimization based on the first-guess departures. Although simple, this bias correction works well in the sense that the CAMS analysis is not biased with respect to MODIS observations. The observation error covariance matrix is assumed to be diagonal, to simplify the problem. The errors are also chosen ad hoc and prescribed as fixed values over land and ocean for the assimilated observations. The aerosol background error covariance matrix used for aerosol analysis was derived using the Parrish and Derber method (also known as NMC method; Parrish and Derber, 1992) as detailed by Benedetti and Fisher (2007). This method was long used for the definition of the background error statistics for the meteorological variables and is based on the assumption that the forecast differences between the 48-h and the 24-h forecasts are a good statistical proxy to estimate the model background errors.

### 3.5.2 Adaptations for DACCIWA

In the operational CAMS runs the prognostic aerosols are not interactive with the clouds or the radiation. Instead a climatology of aerosol optical depths (AODs) is used to model the aerosol direct interaction with radiation. In this sense the prognostic aerosol are not seen by the radiation scheme and do not impact meteorological variables. The aerosol climatology is based at the moment on Tegen et al. 1997 as for the operational IFS run. An effort is ongoing to update this climatology using a calibrated version of the CAMS interim reanalysis (Flemming et al. 2016). The current version of C-IFS does not provide information on the aerosol number concentration as it is based on a bulk model. Both in C-IFS and in the operational IFS, Cloud Condensation Nuclei (CCN) are specified using the following parameterizations. First the near surface aerosol concentration ($Q_a$) is calculated with a parametrization for the injection of aerosol from the surface into the atmosphere based on the 10m wind speed. The formulation follows a parametrization derived for sea salt aerosol concentrations (Erickson et al.1986; Genthon 1992):

$$Q_a = e^{(aW_s+b)} \quad (1),$$

where $W_s$ is the 10m wind speed predicted by the model with coefficients depending on the wind speed ( a=0.16 and b=1.45 for wind speeds less than 15 m $s^{-1}$, and a=0.13 and b=1.89 otherwise). This is applied over both ocean and land, with $Q_a$ limited to a value of 327 µg $m^{-3}$ for wind speeds greater than 30 m $s^{-1}$ over the ocean.

The conversion of aerosol concentration to the number concentration of cloud condensation nuclei then follows an empirical formulation as described by Boucher and Lohmann (1995) among others:

$$CCN = 10^{(c+dLog_{10}Q_a)} \quad (2).$$

In IFS, the coefficients are c=1.2, d=0.5 over ocean and c=2.21, d=0.3 over land.
Morcrette et al. (2011) investigated the use of a CCN parameterization based on the prognostic aerosols following Menon et al. (2002), and showed some impact on meteorological variables. This configuration has not been tested in more recent model versions and hence has not been activated in any of the DACCIWA runs, which implies that the aerosol indirect effect is not modelled. For the

direct effect, however it is possible to activate the prognostic aerosols and make them interactive with the radiation. This has been done for June-July 2014 and 2006 in preparation for the subsequent modelling activities for the year of the field campaign (2016). A total of 4 runs were performed: two control runs for June-July and two experiments with interactive aerosols for the same periods. The resolution of these experiments is T255 which correspond to approximately 80km with 60 vertical levels going up to 0.1hPa. The experiments cover a period of four months from May 2014 to August 2014, allowing one month of spin-up time for the aerosol analysis. The analysis is run twice a day (000UTC and 12UTC) while the forecasts are run out to day 5 as it is in the operational CAMS configuration. Below, we present results from the 2014 runs. For the results from the operational run please see section 3.1 which have been compared with COSMO-ART results.

### 3.5.3 Dataset analysis

Two months of data were analyzed to understand differences between the control run (D12) and the run with interactive aerosols (D13), with specific focus on West Africa (see Tab. 3.5.1).

**Tab. 3.5.1** – Characteristics of the IFS-CAMS model datasets used for this study

| Characteristics | Dataset<br>D12 | D13 |
|---|---|---|
| Time period | 01.06.-31.07.2014 | 01.06.-31.07.2014 |
| Simulation domain | global | global |
| Grid mesh size (km) | 80 (T255) | 80 (T255) |
| Meteorology | IFS | IFS |
| Convection parameterization | yes | yes |
| Cloud microphysics | one-moment bulk | one-moment bulk |
| Aerosol type (online/prescribed) | mineral dust (online), sea salt (online), anthropogenic (online) | mineral dust (online), sea salt (online), anthropogenic (online) |
| Aerosol treatment (bulk/modal/sectional) | bulk for anthropogenic, sectional for natural | bulk for anthropogenic, sectional for natural |
| Direct aerosol effect | no | yes |
| Indirect aerosol effect | no | no |
| Chemistry (online/prescribed, full chemistry) | CAMS, online | CAMS, online |

The first variable evaluated was AOD. Data from the Aerosol Robotic Network (AERONET) are used in the standard verification suite in CAMS for the operational run. The same suite was applied to the DACCIWA 2014 runs. Evaluation metrics include bias and root mean square (RMS) error, among other statistics. In figure 3.5.1 it is possible to see results for July 2014 over Africa. The plot for instantaneous data is noisy and shows virtually no difference in the run with or without interactive aerosols. However, the plots with bias and RMS error as a function of forecast range show that the run with interactive aerosols is slightly better than the control run in terms of lower bias and lower

RMS error, particularly going towards the end of the forecast range. However, a statistical analysis of the significance of this impact has not been performed.

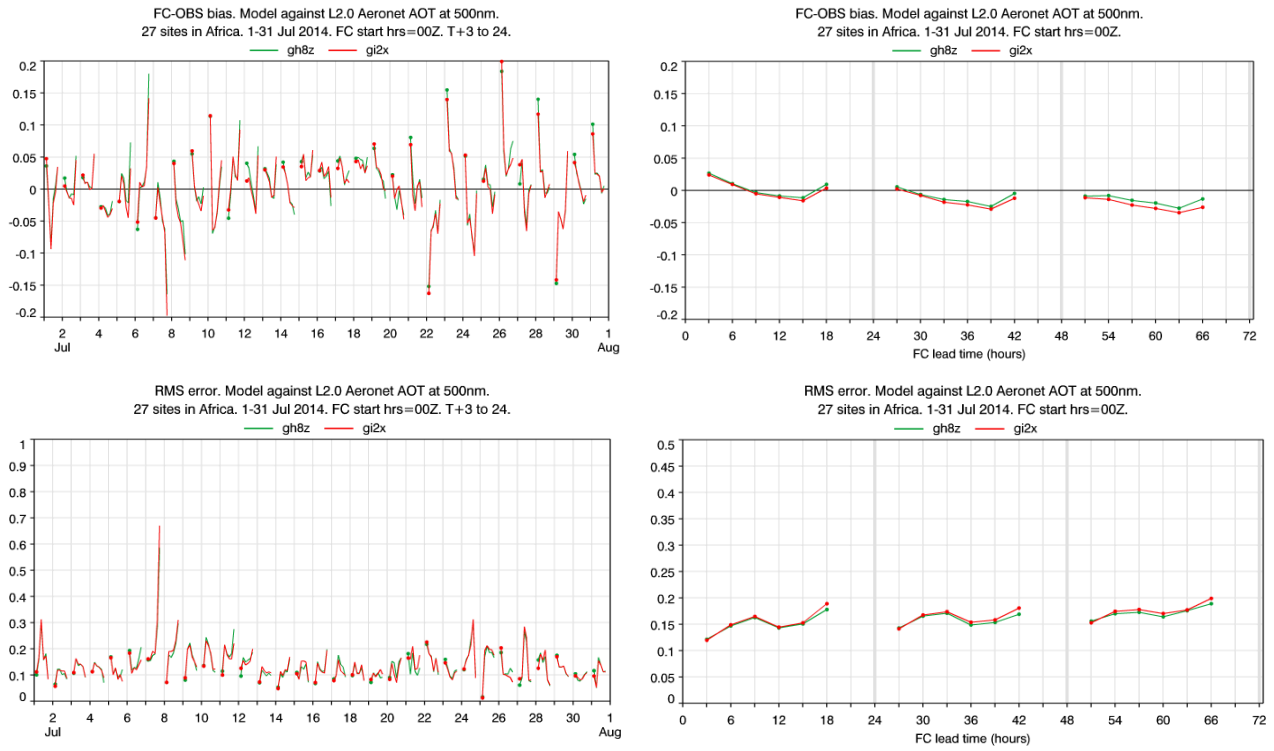


**Fig. 3.5.1** – Comparison of the AOD of D12 (control run, red line) and D13 (interactive aerosol, green line) towards the AERONET AOD at 500nm from 27 sites in Africa for July 2014. Top panels show the bias (forecast minus observations) at coincident times (left) and for the forecast lead time of 72h averaged over July 2014 (right). Bottom panels as top panels but for the root mean square (RMS) error. Model data are interpolated at observation locations.

Figure 3.5.2 shows a comparison of AOD at the Ilorin AERONET station situated in Nigeria (8.4799° N, 4.5418° E). The run with interactive aerosols performs comparably to the standard run and both capture the aerosol variability at Ilorin remarkably well, except for a high AOD case on July 22. Additional AOD data over Benin are being acquired (courtesy of Dr. Aristide Akpo, University of Abomey-Calavi, Cotonou) and will be used for a further evaluation focused over West Africa.

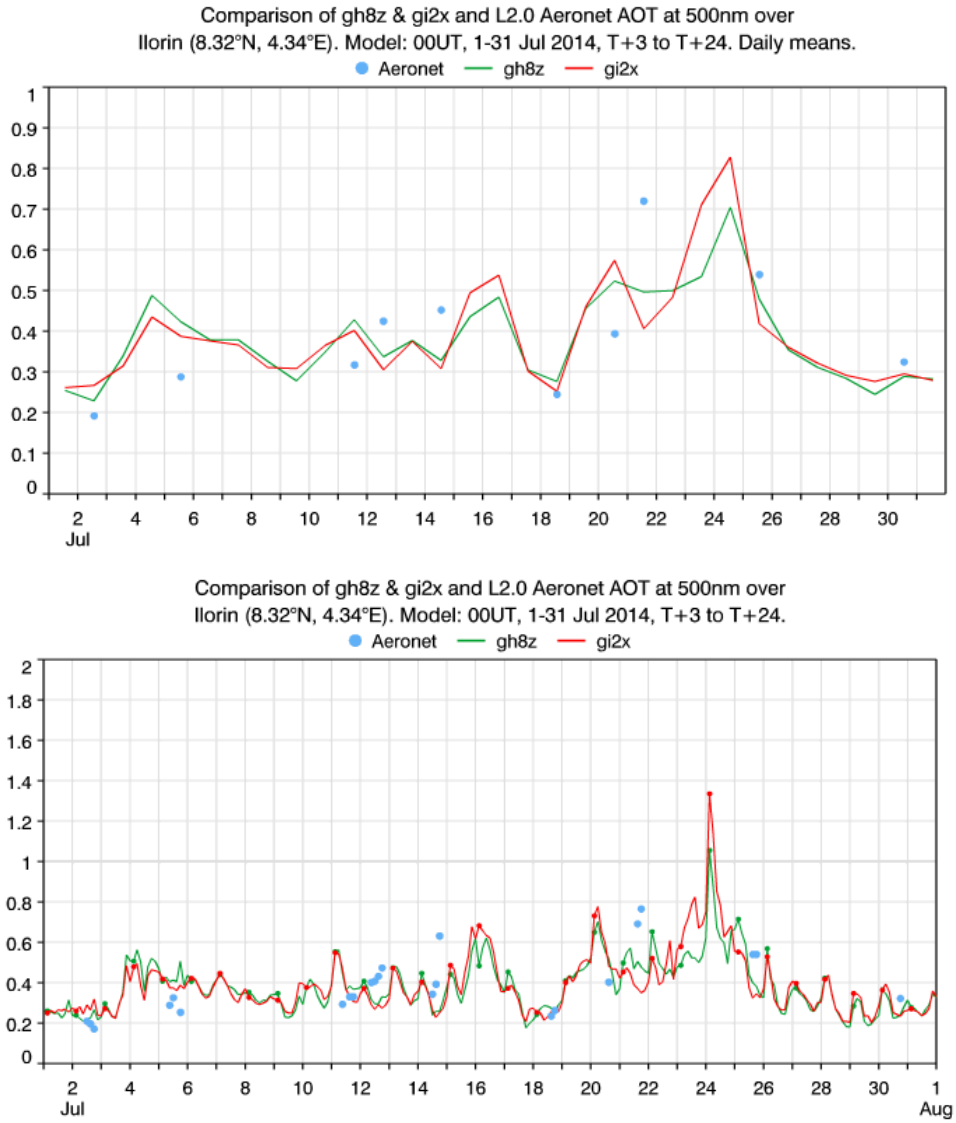


**Fig. 3.5.2** – Comparison of the AOD of D12 (red line) and D13 (green line) towards the AERONET AOD (blue dots) at 500nm for Ilorin (Nigeria) for July 2014. The top panel shows daily means, while the bottom panel shows the instantaneous values.

Figure 3.5.3 shows profiles of cloud cover for June-July 2014, averaged over Box 1. Results show a small impact of the interactive aerosols particularly at 12UTC with an increase in the cloud cover. This is possibly a result of a radiative warming at lower levels and cooling at upper levels connected to the “aerosols of the day” versus climatological values. At 06UTC it is possible to observe well-developed low-level clouds around 925hPa in both runs. The height of the maximum in low-level clouds raises to approx. 850 hPa at 12UTC and is not present in the 1800UTC profile. Similar average plots were obtained for horizontal and meridional winds (not shown), but no impact of the radiatively interactive aerosol was detected.

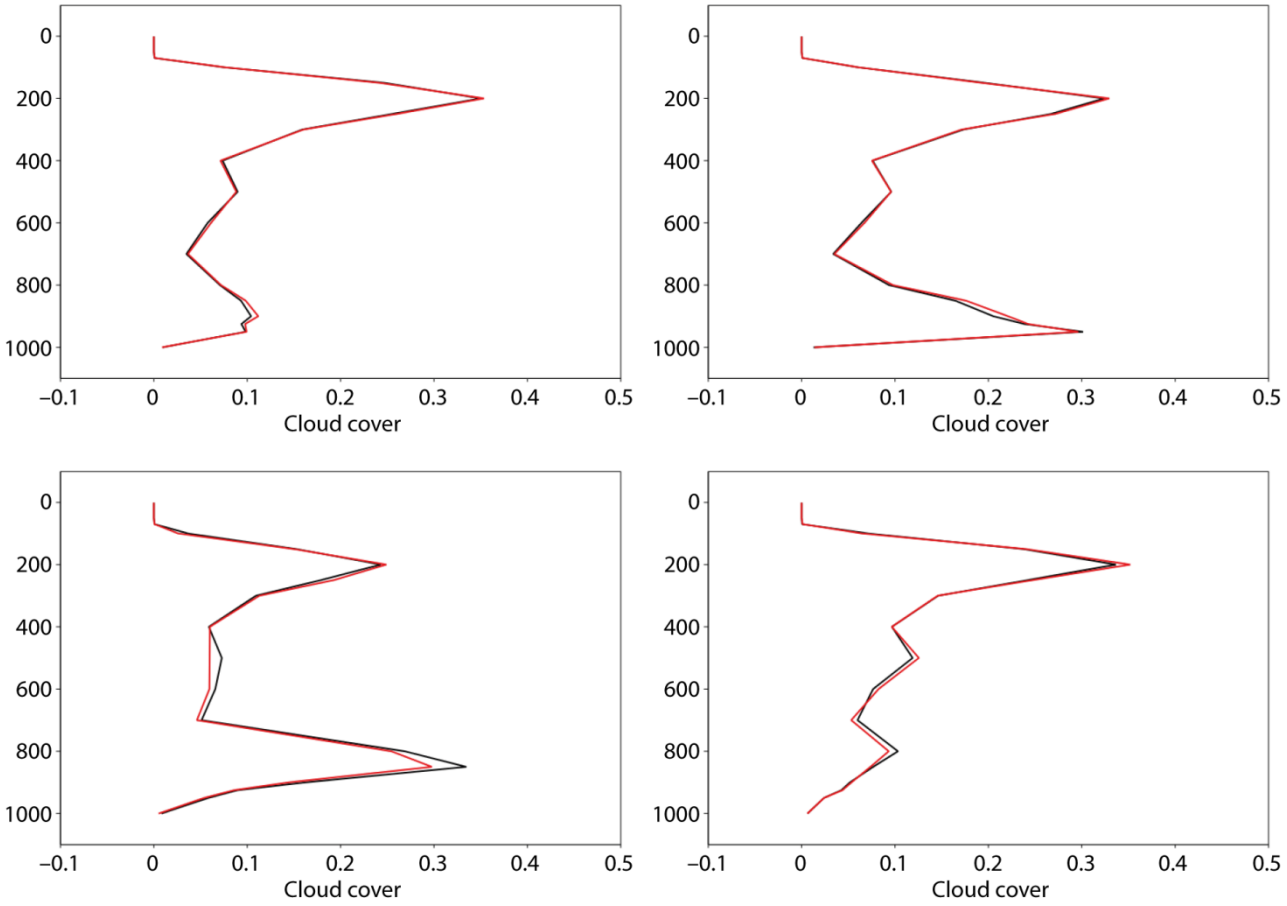


**Fig. 3.5.3** - Cloud cover profiles (vertical axis is pressure in hPa) averaged temporally over June-July 2014 and spatially over Box 1 for D12 (red) and D13 (black). The following analysis times are shown: 00UTC (top left), 06UTC (top right), 12UTC (bottom right) and 18UTC (bottom left).

### 3.5.4 Conclusion

DACCIWA-specific runs were performed with the C-IFS model with the aim to investigate the aerosol direct effect on model parameters over the West African region. A small, positive effect was found in both AODs and average cloud cover. The current runs use standard (global) emission datasets. It would be interesting to repeat the runs with observed emissions from WP2 over West Africa to see if there is a more important aerosol impact on the meteorology. The inclusion of the aerosol indirect effect, although not envisaged during the project, could also be of interest.

## 4. Summary and conclusions

The five models COSMO-ART, UM, CHIMERE, ECHAM-HAM and IFS-CAMS were used to assess the cloud as well as aerosol/chemistry characteristics across SWA. A special focus was set to the characteristics of the nocturnal low-level stratus (NLLS).

**The findings of COSMO-ART** (based on simulations/forecasts for June-July 2016) reveal that the onset, the cloud base height, the diurnal cycle and the regional extent of NLLS is in good agreement with existing model studies (e.g. Schuster et al., 2013) and observations at Savé Supersite obtained during the DACCIWA measurement campaign. The modeling results considering the interaction with prognostic aerosol indicate a reduction of clouds in the lowest layers which has to be analyzed more in detail with additional highly resolved aerosol-interaction simulations.

The aerosol and trace gas spatial distributions simulated by COSMO-ART show good agreement for natural aerosols but have a tendency to overestimate the air pollution from anthropogenic sources compared to remote sensing observations and CAMS chemistry forecasts.

By comparing the results of COSMO-ART and ECHAM-HAM regarding the profile of cloud characteristics averaged over Box 1, similar behavior can be found. Figure 4.1 combines the results of ECHAM-HAM (top, based on Fig. 3.4.6) and COSMO-ART (bottom, based on Fig. 3.1.3 and 3.1.8a,c) to highlight the features in common.

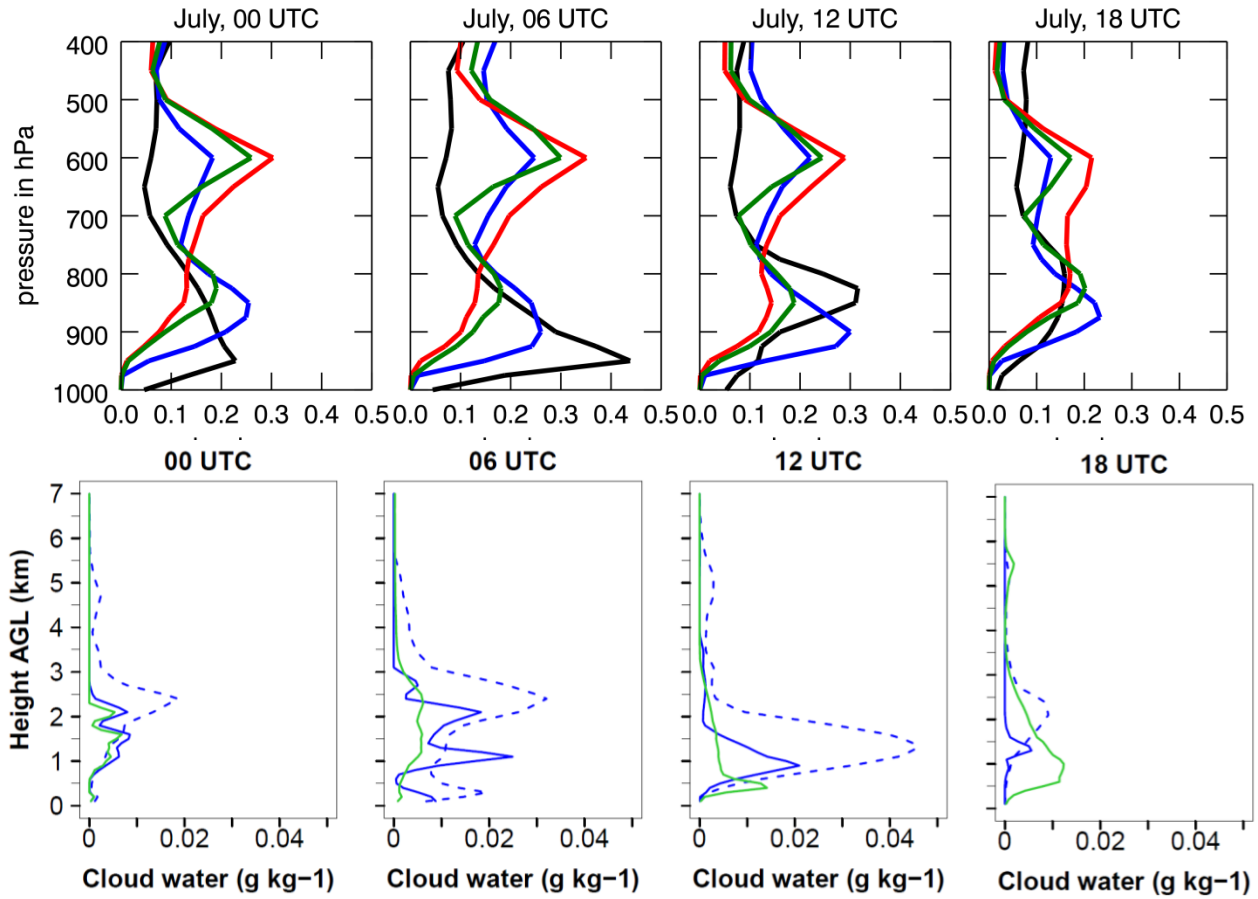


**Fig. 4.1** – Diurnal cycle profile of (top) ECHAM-HAM cloud cover and (bottom) COSMO-ART cloud water (g $kg^{-1}$) spatially averaged over Box 1. Top: ERA-interim (black), D11 (blue, only ECHAM), D10 (red, ACCMIP), D9 (green, ACCMIP+GFAS) for July averaged over 1996-2010. Bottom: D1 averaged from 27 June to 17 July 2016 (dashed blue, Continental domain), D2 for 2 July 2016 (solid blue, Continental domain), D3 for 2 July 2016 (solid green, Regional domain)

Although different parameters and time periods are shown in Figure 4.1, the general pattern can be compared. In the following the focus is on the blue and green lines of the top and bottom row of figures. Top blue line is the ECHAM simulation without interaction with prognostic aerosol (averaged July 1996-2010), bottom blue line is COSMO-ART simulation also without interaction with prognostic aerosol (dashed line is averaged from 27 June to 17 July 2016, solid line is 2 July 2016 only). Top green line is the ECHAM-HAM simulation with interaction with prognostic aerosol (direct and indirect effect) considering anthropogenic and fire emissions (averaged July 1996-2010). Bottom green line is the COSMO-ART simulation with interaction with prognostic aerosol (direct and indirect effect) considering anthropogenic and fire emissions (2 July 2016 only). Therefore, the solid blue lines are the realizations without interaction with prognostic aerosol (I) whereas the solid green lines consider interactions with prognostic aerosols (II).

For 0 UTC we find a peak in cloud cover and cloud water at 1.5km height (850hPa), whereupon in both models the peak is higher for (II). From 0 UTC to 12 UTC the height of the peak decreases for both models but the general trend of a higher peak for (I) persists. At 18 UTC the peak at approx. 1.5km height decreases for (I) in both models, whereas for (II) the amplitude remains the same. Both

models show a double peak structure in the profile which is especially visible at 6 UTC for COSMO-ART but obvious for all time steps of ECHAM-HAM. For ECHAM-HAM, (I) and (II) shows no increased cloud cover in the lowest layers owing to NLLS. COSMO-ART has an increased amount of cloud liquid water at 6 UTC for (I) but not for (II). This leads to the conclusion that for the aerosol interaction simulations ECHAM-HAM produces a NLLS which is too high and without a pronounced diurnal cycle and for COSMO-ART the NLLS disappears when considering the interaction with prognostic aerosol. For the qualitative comparison within Fig. 4.1 we can conclude that the effect of prognostic aerosol on the cloud properties is consistent between ECHAM-HAM and COSMO-ART.
**The findings of UM** (based on forecasts for June-July 2016) show generally a stratiform cloud layer that expanded between 0 UTC and 9 UTC, lifted between 9 UTC and 12 UTC, changed to cumuliform clouds and diluted between 12 UTC and 18 UTC and had a second maximum in cloud coverage and liquid water mixing ratio at 21 UTC.
The UM as well as the COSMO-ART forecasts were used without interactive aerosol or chemistry, but UM was used in a significant higher resolution of 4.4km compared to COSMO-ART (28km) and without convective parameterization. Nevertheless, the diurnal cycle of the NLLS development and transition to cumuliform clouds between 0 and 18 UTC behaves similar in both models (see Fig. 4.2a,b).

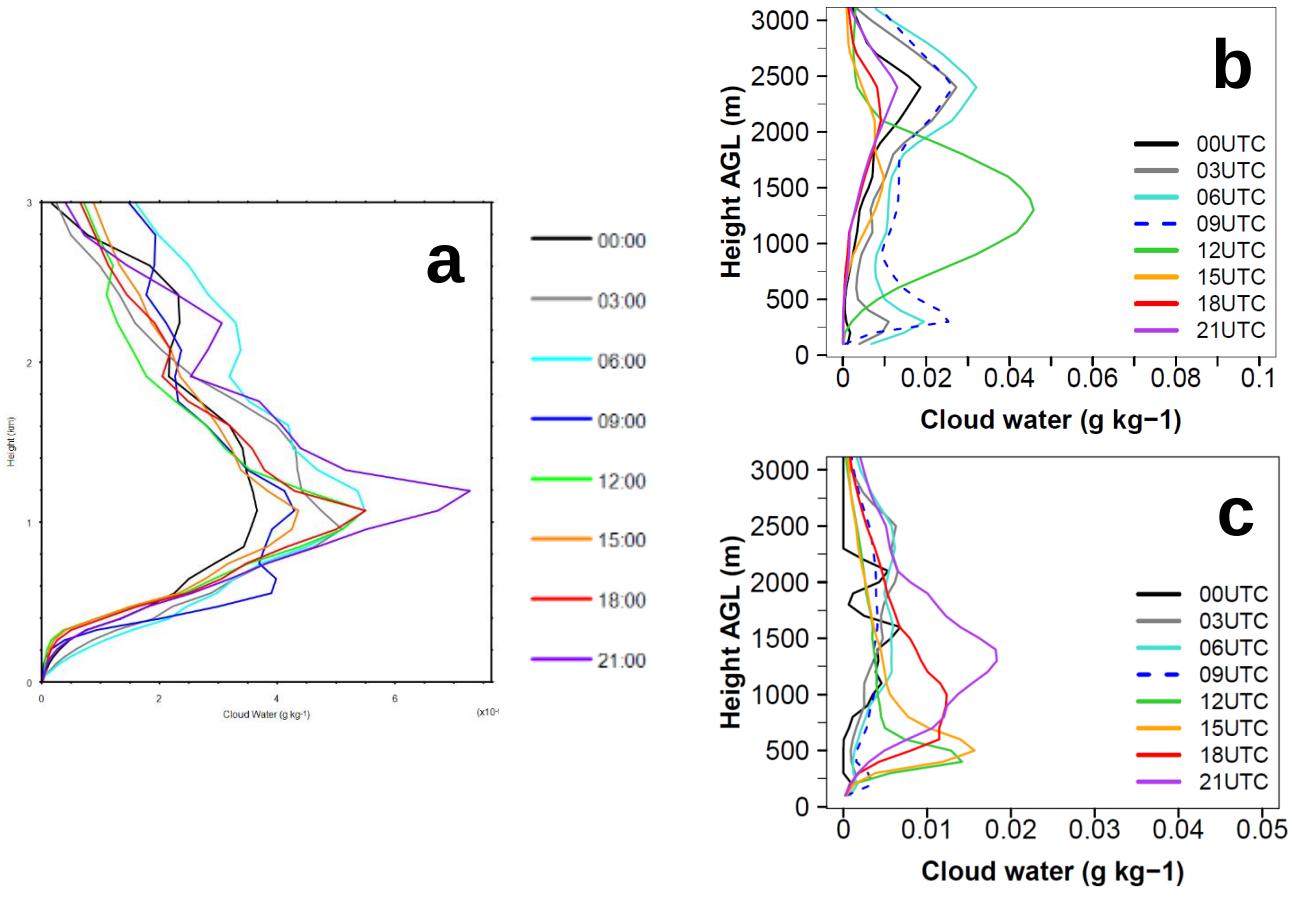


**Fig. 4.2** – Diurnal cycle of cloud liquid water (in g kg$^{-1}$) spatially averaged over Box 1 and temporally averaged from 27 June to 17 July 2016 considering (a) UM (4.4 km grid mesh size, D4) and (b) COSMO-ART (28km grid mesh size, D1) and (right) for 0-3 km height AGL. Additionally, (c) shows the COSMO-ART results for 2 July 2016 with full interaction and 2.5km grid mesh size (D3).
However, for 21 UTC, UM (Fig. 4.2a) has the strongest peak during the diurnal cycle whereas COSMO-ART (Fig. 4.2b) shows no signal at this time of the day. Between 500m and 2000m height, UM shows no decrease in cloud water compared to COSMO-ART. By considering the high resolved COSMO-ART realization for 2 July 2016 (without convective parameterization, Fig. 5.2c) for a comparison with UM, the peak at 21 UTC can be seen in both models at approx. the same height of

1000-1500m. In both models this peak is the strongest of the day. Therefore, Figure 5.2 delivers a first hint of the behavior we can expect from different model setups: (a) highly resolved model with explicit convection and without aerosol interaction, (b) coarse model resolution without explicit convection and without aerosol interaction and (c) highly resolved model with explicit convection and with aerosol interaction. Since the peak at 21 UTC occurs in Fig. 5.2a and 5.2c it is likely related to the higher resolution and the explicit convection rather than the interaction with prognostic aerosol.
The UM forecasting of deep convective systems that may have impacted the flying operations was regarded as good with the initiation locations, propagation and timing of convection tending to match well with reality in the cases investigated.

**The findings of CHIMERE** (based on simulations for May-July 2014) indicate, that the biomass burning emissions represent an important additional factor of air pollution for the urbanized areas of SWA, both for gaseous (ozone and carbon monoxide) and aerosol (PM10). It can be shown that vegetation fires are responsible for an increase in concentrations from 10 to 100% (depending on species and period). The relative contributions from vegetation fires are mainly in the fine mode for primary particulate matter and primary organic matter, but also the aerosol coarse mode for the primary organic matter is non-negligible. This reveals the need for taking into account the vegetation fires in the region of the Gulf of Guinea, even if the source regions were remote. In the ongoing work of DACCIWA, CHIMERE will be online coupled to WRF to study the interaction of the dense biomass burning plumes with convection and precipitation.

**The findings of ECHAM-HAM** (based on simulations for 1996-2010) reveal that the AOT is reproduced reasonably in the model, but the OC and SO4 concentrations seem to be under- and accordingly overestimated during summer times. A comparison of simulated and satellite derived AOT in tropical Savanna indicates that the biomass burning emissions could be overestimated in the GFAS inventory. ECHAM6-HAM2 considers both, the direct and indirect aerosol effects. The 2m temperature is captured well by the coupled model. All simulations are able to simulate the latitudinal location of the rain, but they underestimate the amount of rain south of 10°N. This has to be taken in mind when performing the future projections. The pure climate model simulates the presence of low level clouds at the Guinea Coast. But it does not reproduce their diurnal cycle. The coupled aerosol-climate model underestimates the presence of low level clouds. With use of the GFAS emission inventory the cloud droplet number concentration is higher in low altitudes and some low level clouds are formed.
Together with WP7 the tendencies of temperature and specific humidity will be analyzed, which were provided as additional output from the model. Additionally, the set of ECHAM6-HAM2 AMIP simulations will be expanded. The model will be prepared for the use of the HTAPv2 emission inventory, as well as the inventory developed in DACCIWA WP2 for West Africa.

**The findings of IFS-CAMS** (based on simulations for June-July 2014) indicate a small, positive effect for AOD and averaged cloud cover over the West African region when considering the aerosol direct effect. Since the current realizations are based on standard (global) emission datasets, it is planned to repeat the simulations with the emission inventory derived from WP2 for West Africa. By using the new emission inventory it will be investigated whether there is a more important aerosol impact on meteorology. The inclusion of the aerosol indirect effect, although not envisaged during the project, could also be of interest.

# 5. Literature

## 5.1 COSMO-ART

Athanasopoulou, E., Vogel, H., Vogel, B., Tsimpidi, A., Pandis, S. N., Knote, C., and Fountoukis, C., 2013: Modeling the meteorological and chemical effects of secondary organic aerosol during an EUCAARI campaign, Atmos. Chem. Phys., 13, 625-645, doi:10.5194/acp-13-625-2013.

Athanasopoulou, E., Rieger, D., Walter, C., Vogel, H., Karali, A., Hatzaki, M., Gerasopoulos, E., Vogel, B., Giannakopoulos, C., Gratsea, M., and Roussos, A., 2014: Fire risk, atmospheric chemistry and radiative forcing assessment of wildfires in eastern Mediterranean, Atmos. Environ., 95, 113–125, doi:10.1016/j.atmosenv.2014.05.077.

Baldauf, M., Seifert, A., Förstner, J., Majewski, D., Raschendorfer, M., and Reinhardt, T., 2011: Operational convective-scale numerical weather prediction with the COSMO model: description and sensitivities, Mon. Weather Rev., 139, 3887–3905, doi:10.1175/MWR-D-10-05013.1.

Barahona, D. and Nenes, A., 2009a: Parameterizing the competition between homogeneous and heterogeneous freezing in cirrus cloud formation – monodisperse ice nuclei, Atmos. Chem. Phys., 9, 369–381, doi:10.5194/acp-9-369-2009.

Barahona, D. and Nenes, A., 2009b: Parameterizing the competition between homogeneous and heterogeneous freezing in ice cloud formation – polydisperse ice nuclei, Atmos. Chem. Phys., 9, 5933–5948, doi:10.5194/acp-9-5933-2009.

Deetz, K., Vogel, B., 2016 (under review): Development of a new gas flaring emission data set for southern West Africa, Geosci. Model Dev., doi:10.5194/gmd-2016-110, http://www.geosci-model-dev-discuss.net/gmd-2016-110/.

EDGAR, 2010: http://edgar.jrc.ec.europa.eu/htap_v2/index.php?SECURE=123

Fountoukis, C. and Nenes, A., 2005: Continued development of a cloud droplet formation parameterization for global climate models, J. Geophys. Res.-Atmos., 110, D11212, doi:10.1029/2004JD005591.

GFAS, 2016: http://apps.ecmwf.int/datasets/data/cams-gfas/

Guenther, A. B., Jiang, X., Heald, C. L., Sakulyanontvittaya, T., Duhl, T., Emmons, L. K., Wang, X., 2012: The Model of Emission of Gases and Aerosols from nature version 2.1 (MEGAN2.1): an extended and updated framework of modelling biogenic emissions, Geosci. Model Dev., 5, 1471-1492.

Lana, A., Bell, T. G., Simó, R., Vallina, S. M., Ballabrera-Poy, J., Kettle, A. J., Dachs, J., Bopp, L., Saltzman, E. S., Stefels., J., Johnson, J. E., Liss, P. S., 2011: An updated climatology of surface dimethylsulfide concentrations and emission fluxes in the global ocean, Global Biogeochemical Cycles, Vol. 25, GB1004.

Phillips, V. T., DeMott, P. J., and Andronache, C., 2008: An empirical parameterization of heterogeneous ice nucleation for multiple chemical species of aerosol, J. Atmos. Sci., 65, 2757–2783, doi:10.1175/2007JAS2546.1.

Riemer, N., H. Vogel, B. Vogel (2004), Soot aging time scales in polluted regions during day and night, Atmos. Chem. Phys., 4, 1885–1893, SRef-ID: 1680-7324/acp/2004-4-1885.

Ritter, B. and Geleyn, J.-F., 1992: A comprehensive radiation scheme for numerical weather prediction models with potential applications in climate simulations, Mon. Weather Rev., 120, 303–325, doi:10.1175/1520-0493(1992)120<0303:ACRSFN>2.0.CO;2.

Schuster, R., Fink, A. H., Knippertz, P., 2013: Formation and Maintenance of Nocturnal Low-Level Stratus over the Southern West African Monsoon Region during AMMA 2006, Journal of the Atmospheric Sciences, Vol. 70, 2337-2355.

Seifert, A. and Beheng, K., 2006: A two-moment cloud microphysics parameterization for mixed-phase clouds. part 1: Model description, Meteorol. Atmos. Phys., 92, 45–66, doi:10.1007/s00703-005-0112-4.

Shao, Y., Fink, A. H., Klose, M., 2010: Numerical simulation of a continental-scale Saharan dust event, Journal of Geophysical Research, Vol. 115, D13205.

Stanelle, T., Vogel, B., Vogel, H., Bäumer, D., and Kottmeier, C., 2010: Feedback between dust particles and atmospheric processes over West Africa during dust episodes in March 2006 and June 2007, Atmos. Chem. Phys., 10, 10771–10788, doi:10.5194/acp-10-10771-2010.

Stockwell, W. R., Middleton, P., Chang, J. S., and Tang, X., 1990: The second generation regional acid deposition model chemical mechanism for regional air quality modeling, J. Geophys. Res.-Atmos., 95, 16343–16367, doi:10.1029/JD095iD10p16343.

Rieger, D., Bangert, M., Kottmeier, C., Vogel, H., and Vogel, B., 2014: Impact of aerosol on post-frontal convective clouds over Germany, Tellus B, 66, 22528, doi:10.3402/tellusb.v66.22528.

Vogel, B., Vogel, H., Bäumer, D., Bangert, M., Lundgren, K., Rinke, R., Stanelle, T., 2009: The comprehensive model system COSMO-ART - Radiative impact of aerosol on the state of the atmosphere on the regional scale, Atmos. Chem. Phys., 9, 8661-8680.

Walter, C., Freitas, S. R., Kottmeier, C., Kraut, I., Rieger, D., Vogel, H., Vogel, B. (2016): The importance of plume rise on the concentrations and atmospheric impacts of biomass burning aerosol, Atmos. Chem. Phys., 16, 9201-9219.

World Bank, 2012: http://www.worldbank.org/content/dam/Worldbank/Programs/Top 20 gas flaring countries.pdf, accessed: 5 December 2015.

## 5.2 UM

Boutle, I. A., Abel, S. J., Hill, P. G., Morcrette, C. J., 2014: Spatial variability of liquid clouds and rain: observations and microphysical effects, Q. J. Roy. Met. Soc., 140, Issue 679, 583-594.

Clark, P. A., Harcourt, S. A., Macpherson, B., Mathison, C. T., Cusack, S., and Naylor, M., 2008: Prediction of visibility and aerosol within the operational Met Office Unified Model. i: Model formulation and variational assimilation. Q. J. Roy. Met. Soc., 134, 1801–1816.

Khairoutdinov, M., Kogan, Y., 2000: A New Cloud Physics Parameterization in a Large-Eddy Simulation Model of Marine Stratocumulus, American Meteorological Society, Vol. 128, 229-243

Morgenstern, O., Braesicke, P., O'Connor F. M., Bushell, A.C., Johnson, C. E., Osprey, S. M., Pyle, J. A., 2009: Evaluation of the new UKCA climate-composition model – Part 1: The stratosphere, Geosci. Model Dev., 2, 43-57

O'Connor F. M., Johnson, C. E., Morgenstern, O., Abraham, N. L., Braesicke, P., Dalvi, M., Folberth, G. A., Sanderson, M. G., Telford, P. J., Voulgarakis, A., Young, P. J., Zeng, G., Collins, W. J., Pyle, J. A., 2014: Evaluation of the new UKCA climate-composition model – Part 1: The Troposphere, Geosci. Model Dev., 7, 41-91.

Smith, R. N. B., 1990: A scheme for predicting layer clouds and their water content in a general circulation model, Q. J. Roy. Met. Soc., 116, Issue 492, 435-460.

Wilson, D. R., Bushell, A. C., Kerr-Munslow, A. M., Price, J. D., Morcrette, C. J., 2008: PC2: A prognostic cloud fraction and condensate scheme. I: Scheme description, Q. J. Roy. Met. Soc., 134, Issue 637, 2093-2107.

Wood, N., Staniforth, A., White, A., Allen, T., Diamantakis, M., Gross, M., Melvin, T., Smith, C., Vosper, S., Zerroukat, M., Thuburn, J., 2013: An inherent mass-conserving semi-implicit semi-Lagrangien discretization of the deep-atmosphere global non-hydrostatic equations, Q. J. Roy. Met. Soc., Vol. 140, Issue 682, 1505-1520.

## 5.3 CHIMERE

Alfaro, S.C. and Gomes, L.: Modeling mineral aerosol production by wind erosion: Emission intensities and aerosol size distribution in source areas, J of Geophysical Research, 106, 18,075--18,084, 2001.

Bian, H., and Prather, M.: Fast-J2: accurate simulation of stratospheric photolysis in global chemical models, J Atmos Chem, 41, 281--296, 2002.

Ginoux, P., Chin, M., Tegen, I., Prospero, J.~M., Holben, B., Dubovik, O., and Lin, S.J.: Sources and distributions of dust aerosols simulated with the GOCART model, Journal of Geophysical Research, 106, 20255--20273, 2001.

Hauglustaine, D.A., Balkanski, Y., and Schulz, M.: A global model simulation of present and future nitrate aerosols and their direct radiative forcing of climate, Atmos Chem Phys, 14, 6863--6949, 10.5194/acpd-14-6863-2014, 2014.

Janssens-Maenhout, G., Crippa, M., Guizzardi, D., Dentener, F., Muntean, M., Pouliot, G., Keating, T., Zhang, Q., Kurokawa, J., Wankmuller, R., Denier van der Gon, H., Kuenen, J. J.P., Klimont, Z., Frost, G., Darras, S., Koffi, B., and Li, M.: HTAP v2.2: a mosaic of regional and global emission grid maps for 2008 and 2010 to study hemispheric transport of air pollution, Atmospheric Chemistry and Physics, 15, 11411–11432, 10.5194/acp-15-11411-2015, 2015.

Mailler, S., Menut, L., Khvorostyanov, D., Valari, M., Couvidat, F., Siour, G., Turquety, S., Briant, R., Tuccella, P., Bessagnet, B., Colette, A., Letinois, L., and Meleux, F.: CHIMERE-2016: From urban to hemispheric chemistry-transport modeling, Geoscientific Model Development Discussions, 2016, 1--41, 10.5194/gmd-2016-196, www.geosci-model-dev-discuss.net/gmd-2016-196, 2016.

Menut, L., C. Schmechtig, and B. Marticorena: Sensitivity of the sandblasting fluxes calculations to the soil size distribution accuracy, Journal of Atmospheric and Oceanic Technology, 22, 1875--1884, 2005.

Menut, L., Bessagnet, B., Khvorostyanov, D., Beekmann, M., Blond, N., Colette, A., Coll, I., Curci, G., Foret, F., Hodzic, A., Mailler, S., Meleux, F., Monge, J., Pison, I., Siour, G., Turquety, S., Valari, M., Vautard, R., and Vivanco, M.: CHIMERE 2013: a model for regional atmospheric composition modelling, Geoscientific Model Development, 6, 981–1028, 10.5194/gmd-6-981-2013, 2013.

Menut, L., Perez Garcia-Pando, C., Haustein, K., Bessagnet, B., Prigent, C., and Alfaro, S.: Relative impact of roughness and soil texture on mineral dust emission fluxes modeling, J Geophys Res, 118, 6505–6520, 10.1002/jgrd.50313, 2013.

Rea, G., Turquety, S., Menut, L., Briant, R., Mailler, S., and Siour, G.: Source contributions to 2012 summertime aerosols in the Euro-Mediterranean region, Atmospheric Chemistry and Physics, 15, 8013–8036, 10.5194/acp-15-8013-2015, www.atmos-chem-phys.net/15/8013/2015/, 2015.

Turquety, S., Menut, L., Bessagnet, B., Anav, A., Viovy, N., Maignan, F., and Wooster, M.: APIFLAME v1.0: High resolution fire emission model and application to the Euro-Mediterranean region}, Geoscientific Model Development, 7, 587--612, 10.5194/gmd-7-587-2014, 2014.

Wild, O., Zhu, X., and Prather, M.~J.: Fast-J: Accurate Simulation of In- and Below-Cloud Photolysis in Tropospheric Chemical Models, J. Atmos. Chem., 37, 245--282, 2000.

*ECHAM*

Heald, C. L. Coe, H., Jimenez, J. L., Weber, R. J., Bahreini, R., Middlebrook, A. M., Russell, L. M., Jolleys, M., Fu, T.-M., Allan, J. D., Bower, K. N., Capes, G., Crosier, C., Morgan, W. T., Robinson, N. H., Williams, P. I., Cubinson, M. J., DeCarlo, P. F., Dunlea, E. J., 2011: Exploring the vertical profile of atmospheric organic aerosol: comparing 17 aircraft field campaigns with a global model, Atmos. Chem. Phys., 11, 12673-12696

Heil, A., J. W. Kaiser, G. R. van der Werf, M. J. Wooster, M. G. Schultz, and H. Dernier van der Gon, 2010: Assessment of the real-time fire emissions (GFASv0) by MACC, Tech. Memo, 628, ECMWF, Reading, UK, 2010

Iacono, M. J., J. S. Delamere, E. J. Mlawer, M. W. Shephard, S. A. Clough, and W. D. Collins, 2008: Radiaitve forcing by long-lived greenhouse gases: Calculations with the AER radiative transfer models, J. Geophys. Res., 113, D13103, doi:10.1029/2008JD0099443

Lamarque, J.-F., T. C. Bond, V. Eyrin, C. Granier, A. Heil, Z. Klimont, D. Lee, C. Liousse, A. Mieville, B. Owen, M. G. Schultz, D. Shindell, S. J. Smith, E. Stehfest, J. Van Aardenne, O. R. Cooper, M. Kainuma, N.

Mahowald, J. R. McConnell, V. Naik, K. Riahi, and D. P. van Vuuren, 2010: Historical (1850-2000) gridded anthropogenic and biomass burning emissions of reactive gases and aerosols: methodology and application, Atmos. Chem. Phys., 10, 7017-7039, doi:10.5194/acp-10-7017-2010, 2010.

Lin, S. J. and R. B. Rood, 1996: Multidimensional flux-form semi-Lagrangian transport schemes, Mon. Weather Rev., 124, 2046-2070.

Lohmann, U. and E. Roeckner, 1996: Design and performance of a new cloud microphysis scheme developed for the ECHAM general circulation model, Climate Dnamics, 12, 557-572.

Roeckner, E., G. Baeuml, L. Bonventura, R. Brokopf, M. Esch, M. Giorgetta, S. Hagemann, I. Kirchner, L. Kornblueh, E. Manzini, . Rhodin, U. Schlese, U. Schulzweida, A. Tomkins, 2003: The atmospheric general circulation model ECHAM5. Part I: Model description, Report 349, Max Planck Institute for Meteorology, Hamburg, Germany.

Stevens, B., M. Giorgetta, M. Esch, T. Mauritsen, T. Crueger, S. Rast, M. Salzmann, H. Schmidt, J. Bader, K. Block, R. Brokopf, I. Fast, S. Kinne, L. Kornblueh, U. Lohmann, R. Pincus, T. Reichler,, and E. Roeckner, 2013: Atmospheric component of the MPI-M Earth System Model: ECHAM6, James, 5, 146-172, doi:10.1002/jame.20015.

Stier, P., J. Feichter, S. Kinne, S. Kloster, E. Vignati, J. Wilson, L. Ganzeveld, I. Tegen, M. Werner, Y. Balkanski, M. Schulz, O. Boucher, A. Minikin, and A. Petzold, 2005: The aerosol-climate model ECHAM5-HAM, Atmos. Chem. Phys., 5, 1125-1156.

Vignati, E., J. Wilson, and P. Stier, 2004: An efficient size-resolved aerosol microphysics module for large-scale aerosol transport models, J. Geophys. Res., 109, D22202, doi:10.1029/2003JD004485.

Zhang, K., D. O'Donnell, J. Kazil, P. Stier, S. Kinne, U. Lohmann, S. Ferrachat, B. Croft, J. Quaas, H. Wan, S. Rast, and J. Feichter, 2012: The global aerosol-climate model ECHAM-HAM, version 2: sensitivity to improvements in process representations, Atmos. Chem. Phys., 12, 8911-8949, doi:10.5194/acp-12-8911-2012.

## 5.4 IFS-CAMS

Benedetti, A., and M. Fisher, 2007: Background error statistics for aerosols, Q. J. R. Meteorol. Soc., 133, 391–405.

Benedetti, A., J.-J. Morcrette, O. Boucher, A. Dethof, R. J. Engelen, M. Fischer, H. Flentjes, N. Huneeus, L. Jones, J. W. Kaiser, S. Kinne, A. Mangold, M. Razinger, A. J. Simmons, M. Suttie, and the GEMS-AER team, Aerosol analysis and forecast in the ECMWF Integrated Forecast System. Part II : Data assimilation, Journal of Geophysical Research, 114, D13205, doi:10.1029/2008JD011115, 2009. http://onlinelibrary.wiley.com/doi/10.1029/2008JD011115/abstract

Boucher, O. and Lohmann, U.: The sulfate-CCN-cloud albedo effect: A sensitivity study with two general circulation models,Tellus, Ser. B, 47, 281–300, 1995

Boucher, O., M. Pham, and C. Venkataraman, 2002: Simulation of the atmospheric sulfur cycle in the LMD GCM: Model description, model evaluation, and global and European budgets, Note 23, 26 pp., Inst. Pierre-Simon Laplace, Paris, France. (Available at http://icmc.ipsl.fr/images/publications/scientific_notes/note23.pdf)

Dee, D. and S. Uppala, 2008: Variational bias correction in ERA-Interim, ECMWF, Technical Memorandum 575, p. 26. Available at: http://www.ecmwf.int/publications/library/do/references/show?id=88715

Dentener, F., et al., 2006: Emissions of primary aerosol and precursor gases in the years 2000 and 1750 prescribed data-sets for AeroCom, Atmos. Chem. Phys., 6, 4321 – 4344. (Available at http://www.atmoschem-phys.net/6/4321/2006/acp-6-4321-2006.pdf)

Erickson, D. J., Merril, J. T., and Duce, R. A., 1986. Seasonal estimates of global atmospheric sea-salt distributions. J Geophys. Res., 91, 1067-1072.

Flemming, J., Benedetti, A., Inness, A., Engelen, R., Jones, L., Huijnen, V., Remy, S., Parrington, M., Suttie, M., Bozzo, A., Peuch, V.-H., Akritidis, D., and Katragkou, E.: The CAMS interim Reanalysis of Carbon Monoxide, Ozone and Aerosol for 2003–2015, Atmos. Chem. Phys. Discuss., doi:10.5194/acp-2016-666, in review, 2016.

Genthon, C., 1992: Simulations of desert dust and sea salt aerosols in Antarctica with a general circulation model of the atmosphere.Tellus, 44B, 371-389.

Guelle, W., M. Schulz, Y. Balkanski, and F. Dentener, 2001: Influence of the source formulation on modeling the atmospheric global distribution of the sea salt aerosol, J. Geophys. Res., 106, 27,509– 27,524.

Kaiser, J.W., A. Heil, M.O. Andreae, A. Benedetti, N. Chubarova, L. Jones, J.-J.Morcrette, M. Razinger, M.G. Schultz, M. Suttie, and G.R. van der Werf, 2011: Biomass burning emissions estimated with a global fire assimilation system based on observed fire radiative power. Biogeosciences Discuss., 8(4), 7339-7398.

Mangold, A., H. De Backer, B. De paepe, D. Ceburnis, I. Chiapello, Y. Derimian, H. Flentje, N. Huneeus, S. Kinne, J.-J. Morcrette, A. Benedetti, O. Boucher, 2010: Aerosol analysis and forecast in the ECMWF Integrated Forecast System. Part III: Evaluation by means of case studies, Journal of Geophysical Research, 116, D03302, doi:10.1029/2010JD014864, 2011. LINK TO http://onlinelibrary.wiley.com/doi/10.1029/2010JD014864/abstract

Mann, G.W., K.S. Carslaw, D.V. Spracklen, D.A. Ridley, P.T. Manktelow, M.P. Chipperfield, S.J. Pickering, and C.E. Johnson, 2010: Description and evaluation of GLOMAP-mode: a modal global aerosol microphysics model for the UKCA composition-climate model, Geosci. Model Dev., 3, 519-551, doi10.5194/gmd-3-519-2010. LINK TO http://www.geosci-model-dev.net/3/519/2010/gmd-3-519-2010.html

Menon, S., A.D. Del Genio, D. Koch, and G. Tselioudis, 2002: GCM simulations of the aerosol indirect effect: Sensitivity to cloud parameterization and aerosol burden.J. Atmos. Sci.,59, 692-713.

Monahan, E. C., D. E. Spiel, and K. L. Davidson, 1986: A model of marine aerosol generation via whitecaps and wave disruption, in Oceanic Whitecaps, edited by E. C. Monahan and G. MacNiocaill, pp. 167–174, D. Reidel, Norwell, Mass.

Morcrette, J.-J., A. Beljaars, A. Benedetti, L. Jones, and O. Boucher, 2008: Sea-salt and dust aerosols in the ECMWF IFS model , Geophys. Res. Lett., 35, L24813, doi:10.1029/2008GL036041

Morcrette, J.-J., O. Boucher, L. Jones, D. Salmond, P. Bechtold, A. Beljaars, A. Benedetti, A. Bonet, J. W. Kaiser, M. Razinger, M. Schulz, S. Serrar, A. J. Simmons, M. Sofiev, M. Suttie, A. M. Tompkins, and A. Untch, 2009: Aerosol analysis and forecast in the ECMWF Integrated Forecast System. Part I: Forward modelling, Journal of Geophysical Research, 114D, D06206, doi:10.1029/2008JD011235, 2009. http://onlinelibrary.wiley.com/doi/10.1029/2008JD011235/abstract

Morcrette, J.-J, Benedetti, A., Ghelli, A., Kaiser, J.W., and A.M. Tompkins, 2011: Aerosol-Cloud-Radiation Interactions and their Impact on ECMWF/MACC Forecasts. Technical Memo 660, available at http://www.ecmwf.int/sites/default/files/elibrary/2011/11283-aerosol-cloud-radiation-interactions-and-their-impact-ecmwfmacc-forecasts.pdf

Parrish, D. F., and J. C. Derber, 1992: The National Meteorological Center's spectral statistical-interpolation analysis system, Mon. Weather Rev.,120, 1747– 1763.

Reddy, M. S., O. Boucher, N. Bellouin, M. Schulz, Y. Balkanski, J.-L.Dufresne, and M. Pham (2005), Estimates of global multicomponent aerosol optical depth and direct radiative perturbation in the Laboratoire de Météorologie Dynamique general circulation model, J. Geophys. Res.,110, D10S16, doi:10.1029/2004JD004757.

Schulz, M., G. de Leeuw, and Y. Balkanski, 2004: Sea-salt aerosol source functions and emissions, in Emission of Atmospheric Trace Compounds, edited by C. Granier, P. Artaxo, and C. E. Reeves, pp. 333–354, Kluwer Acad., Norwell, Mass.

Tegen, I., P. Hoorig, M. Chin, I. Fung, D. Jacob, and J. Penner 1997: Contribution of different aerosol species to the global aerosol extinction optical thickness: Estimates from model results,J. Geophys. Res.,102, 23,895–23,915.

Tompkins, A. M., 2005: A revised cloud scheme to reduce the sensitivity to vertical resolution, Tech. Memo. 0599, 25 pp., Res. Dep., Eur. Cent. for Medium-Range Weather Forecasts, Reading, UK.